JOURNAL OF COASTAL AND HYDRAULIC STRUCTURES

Experimental study on a breaking-enforcing breakwater

Joep van der Zanden[1], Arne van der Hout[2,3], William Otto[1], Floor Spaargaren[1], Brenda Walles[4], and Jaap de Wilde[1]

Abstract

Floating breakwaters are moored structures that attenuate wave energy through a combination of reflection and dissipation. Studies into floating breakwaters have been generally restricted to optimising the attenuation performance. This study presents a novel floating breakwater type that was developed to have good attenuation performance while keeping wave drift loads as small as possible. The floating breakwater was designed as a submerged parabolic beach that enforces wave energy dissipation through breaking. The design was tested in a 3D shallow-water wave basin in captive and moored setups for regular and irregular wave conditions. Results are presented in terms of attenuation performance, motions, and (mooring) loads. The results show that the breaking of waves improves the attenuation performance of the floater in captive setup. However, in moored setup, the attenuation performance was dominated by diffraction and radiation of the wave field, with breaking being of secondary importance. This shows that breaking-enforcing floating breakwaters have potential, but require a high vertical hydrostatic and/or mooring stiffness in order to enforce intense breaking. Mean wave drift loads on the object showed significant difference between breaking and non-breaking waves in both setups, with breaking waves leading to lower normalized loads. This is attributed to breaking-induced set-up and set-down of the water level. As a result, the new breakwater design has a more favourable balance between wave attenuation and drift loads than common (i.e., box-, pontoon-, or mat-type) floating breakwater designs. Tests with varying surface roughness showed that floating breakwaters may benefit from dual-use functions that naturally increase the roughness (e.g., shellfish, vegetation), which have a marginal effect on the attenuation performance, but increase the added mass and hydrodynamic damping and as such, reduce mooring line loads.

Keywords:

[1]j.v.d.zanden@marin.nl, w.otto@marin.nl, f.spaargaren@marin.nl, j.dewilde@marin.nl, Maritime Research Institute Netherlands (MARIN), The Netherlands
[2]arne.vanderhout@deltares.nl, Deltares, The Netherlands
[3]TU Delft, CiTG, Ports & Waterways, the Netherlands
[4]brenda.walles@wur.nl, Wageningen Marine Research, The Netherlands

1   Introduction

Breakwaters are fixed or floating structures that attenuate the energy of incident waves by means of reflection and/or dissipation, hence providing a shelter against wave action. Breakwaters are applied in near-shore and offshore areas, typically to secure economic activities (e.g., harbours, waterways, aquaculture, offshore operations) or to protect coastal regions against erosive wave action that can lead to the loss of vital habitats and, at long term, threaten inland safety. Floating breakwaters are buoyant structures, moored to the sea bed. Compared to fixed breakwaters, floating breakwaters have lower environmental and visual impact, are more flexible in terms of installation and rearrangement, and present an economically attractive alternative in areas with poor foundation opportunities (e.g., deep water or soft soils) (Brebner and Ofuya, 1968; McCartney, 1985). However, floating breakwaters are also more subject to structural-fatigue issues and require a careful design to local environmental conditions (Hales, 1981). Comprehensive reviews of existing floating breakwater designs and performance can be found (Hales, 1981; McCartney, 1985; Burcharth et al., 2015; Dai et al., 2018); a concise summary is presented here.

Conventional floating breakwaters include box-type, pontoon-type, and mat-type designs that float at the water surface (McCartney, 1985; Burcharth et al., 2015). Box-type breakwaters consist of solid boxes, commonly engineered from concrete, which attenuate the incident wave energy through reflection. Appurtenances to the box-shaped structure, e.g., horizontal or vertical plates, may promote wave energy attenuation through dissipation and increase the hydrodynamic damping of the structure's motions (Huang et al., 2014; Burcharth et al., 2015; Christensen et al., 2018; Zhang et al., 2018; Liu et al., 2019). The effectiveness of floating breakwaters reduces for waves that are considerably longer than the structure (in longitudinal direction of wave propagation) (McCartney, 1985; Koutandos et al., 2004; Peña et al., 2011). In order to improve the effectiveness for longer waves against limited material costs, structures with relatively high width to volume ratio have been developed, commonly referred to as pontoon-type breakwaters (Burcharth et al., 2015). Mat-type floating breakwaters are generally fabricated from relatively cheap material such as old tyres (McGregor and Gilbert, 1982) or brushwood (van Steeg and van Wesenbeeck, 2011). These breakwaters attenuate waves through dissipation, hence requiring a large surface area to be effective. This, in combination with their visual impact, is considered the primary downside of mat-type breakwaters (Burcharth et al., 2015).

While aforementioned studies involved structures floating at the water surface, other studies have assessed the attenuating performance of structures that are completely submerged. These studies include structures shaped as a box (Rahman et al., 2006; Peng et al., 2013; Verduzco-Zapata et al., 2017), a horizontal plate (Verduzco-Zapata et al., 2017; Cheng et al., 2017; He et al., 2019), or differently (Liu and Wang, 2020a,b). Submerged floating breakwaters have limited visual impact (Verduzco-Zapata et al., 2012) and can trigger breaking of the incident wave, which, analogous to fixed submerged breakwaters (Postacchini et al., 2011), considerably improves the attenuation performance (Liu and Wang, 2020b).

Floating breakwaters are held in place by mooring lines or piles, with piled mooring being suitable only at shallow sites (McCartney, 1985). The mooring lay-out requires careful design to environmental conditions, not only from a structural and mooring integrity point of view, but also because the mooring stiffness affects the attenuation performance of the breakwater (Loukogeorgaki et al., 2017). A stiffer mooring system tends to lead to better wave attenuation performance (Loukogeorgaki and Angelides, 2005). Consistently, a captive setup (all degrees of motions restrained) or piled setup (structure can only move vertically) generally induce stronger wave attenuation than a moored setup (Ruol et al., 2012). However, for a dissipative structure, Ji et al. (2018) found higher attenuation for wave frequencies corresponding to one of the natural frequencies of the moored floater, which is attributed to enhanced viscous dissipation induced by resonant motion behaviour. At the same time, resonant motion behaviour leads to high instantaneous mooring loads (Loukogeorgaki and Angelides, 2005) and it is therefore recommended to design the mooring system based on second-order rather than first-order wave excitation (Drimer et al., 1992).

The cost-effectiveness of floating breakwaters can be improved when they accommodate secondary services next to their primary function of wave attenuation. Such secondary services may include aquaculture (Murali and Mani, 1997; Dong et al., 2008; Tang et al., 2011; Ji et al., 2018) or wave energy harvesting (He et al., 2012; Zhao et al., 2019). Observations on foreshores, reefs, and in laboratory have shown that vegetation and shellfish can enhance wave energy dissipation (e.g., Borsje et al., 2011; Walles, 2015; Jacobsen et al., 2019; Vuik et al., 2019). The present study explores the potential of employing such 'ecological engineering' modes for wave attenuation in the design of a floating breakwater.

Most previous studies focused largely on the attenuation performance and first order motions of floating

breakwater designs in regular wave conditions. However, for mooring integrity and application in irregular seas, also second order wave loads are significant. The present study aims to develop and assess a novel floating breakwater which results in relatively high wave attenuation against low mooring loads. This is realised through a parabolic beach shaped floater that enforces the incident waves to break. The new design is assessed in terms of wave attenuation and (mooring) loads through physical experiments, with the structure tested in captive as well as moored setup. The experimental results are complemented by linear wave diffraction calculations, which are primarily aimed at understanding the three-dimensional wave field around the structure.

The paper is organised as follows. Section 2 presents the main considerations motivating the design of the floater and mooring. The experiments and diffraction calculations are described in Section 3. The results are presented in Section 4 (motion behaviour), Section 5 (attenuation performance), and Section 6 (loads on floater and mooring). Section 7 presents a discussion and outlook, followed by the main conclusions in Section 8.

2   Design of floating breakwater

The floating breakwater in the present study was designed to yield relatively high wave attenuation against low wave drift loads. By doing so, the costs of mooring can be reduced and the cost-effectiveness of the design is promoted. The present section summarizes the main considerations that led to the breakwater design.

2.1   Theoretical considerations

The time-averaged force by waves encountering an object is commonly referred to as the wave drift load. The drift load is explained through second-order processes related to wave diffraction, with forces scaling to the squared amplitude of the incident wave, and it can be derived from potential flow theory (for more background, see, e.g., Faltinsen and Loken, 1978; Pinkster, 1979; Sarpkaya and Isaacson, 1981). A theoretical review on drift loads that is especially relevant for the present study was provided by Longuet-Higgins (1977).

From conservation of momentum fluxes, the wave drift load $F_{\rm d}$ per unit width W on a floating body can be expressed as (Longuet-Higgins, 1977):

$$\frac{F_{\rm d}}{W} = \frac{1}{4}\rho g[1 + \frac{2kh}{\sinh 2kh}](a_{\rm i}^2 + a_{\rm r}^2 - a_{\rm t}^2) \tag{1}$$

where ρ is the water density; g is the gravitational acceleration; k is the wave number; h is the water depth; and $a_{\rm i}$, $a_{\rm r}$, and $a_{\rm t}$ are the incident, reflected, and transmitted wave amplitudes, respectively. The drift load $F_{\rm d}$ depends on the degree of reflection and 'absorption' of wave energy, where the latter can be interpreted as the wave energy that is translated to body motions or is dissipated into heat through viscous drag.

For fully reflective structures, assuming no energy absorption ($a_{\rm i}^2 = a_{\rm r}^2 + a_{\rm t}^2$), Eq. 1 can be rewritten to (see also Maruo, 1960):

$$\frac{F_{\rm d}}{W} = \frac{1}{2}\rho g a_{\rm i}^2[1 + \frac{2kh}{\sinh 2kh}](1 - K_{\rm t}^2) \tag{2}$$

Here, $K_{\rm t} = a_{\rm t}/a_{\rm i}$ is the wave transmission coefficient. If, on the other hand, wave reflection is negligible ($a_{\rm r}^2 = 0$), Eq. 1 simplifies to:

$$\frac{F_{\rm d}}{W} = \frac{1}{4}\rho g a_{\rm i}^2[1 + \frac{2kh}{\sinh 2kh}](1 - K_{\rm t}^2) \tag{3}$$

The factor two difference between both equations arises because the incident momentum is either reflected (Eq. 2) or absorbed (Eq. 3). This implies that reflective breakwaters will experience higher drift loads than 'absorbing' (more generally referred to as dissipating) breakwaters. In the present study, rather than dissipating energy through friction, the primary wave attenuation mechanism is wave breaking. This choice is justified based on two grounds.

Firstly, breaking waves produce large rotational vortices which transform wave energy into turbulent energy that is eventually dissipated into heat (Peregrine, 1983). This results in high wave energy dissipation rates

per horizontal area, hence overcoming the drawback of most existing friction-based (e.g., mat-type) floating breakwaters that require a large surface area.

Secondly, experimental results presented by Longuet-Higgins (1977) showed that the wave drift loads exerted by waves propagating over a submerged structure reduce considerably, and can even reverse direction, when the waves break. As such, the drift loads deviate strongly from the predictions by Eq. 1. This is in part explained because the breaking-induced dissipation comes into play as an additional term in the momentum flux and wave energy balances. Further, wave breaking leads to a spatial gradient in the time-averaged water level, caused by spatial variations in the wave radiation stress across the breaking region (Longuet-Higgins and Stewart, 1964). For waves breaking over a submerged object, the mean water level gradient exerts a net force on the object in addition to the drift loads that follow from potential flow theory (Longuet-Higgins, 1977).

2.2 Design of floater

A sketch of the floater design is shown in Figure 1. The figure features designation of key parameters describing the geometry, including the floater draft depth T_{f}, depth D_{f}, length L_{f}, thickness t_{f}, and minimum water depth above the floater h_0.
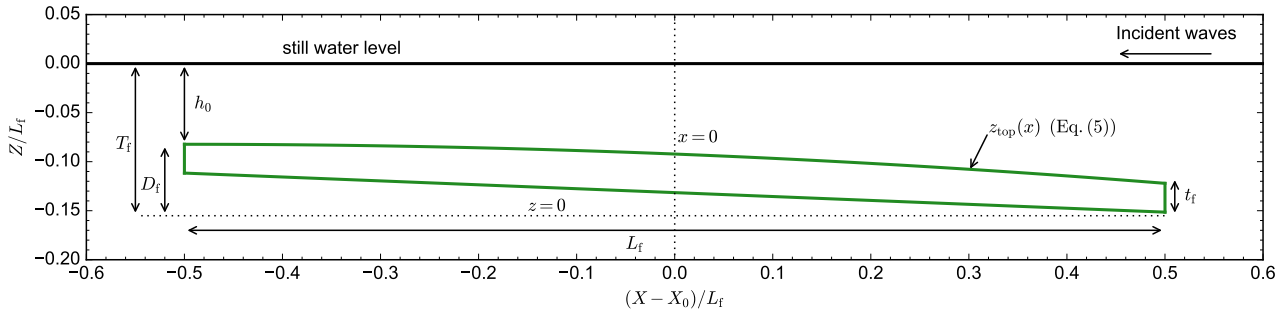

Figure 1: Sketch of floater design including designation of parameters. The dotted lines mark the horizontal and vertical datum of the local (model-fixed) coordinate system.

Waves propagating onto a progressively decreasing water depth increase in height, because the wave celerity decreases while the momentum flux remains constant (Svendsen, 1984). This process, termed shoaling, further leads to waves becoming increasingly horizontally and vertically asymmetric, due to amplitude and phase changes of the higher harmonics of the wave (Phillips, 1960; Flick et al., 1981), ultimately leading to instability and breaking. Hence, an effective way to promote breaking is by enforcing waves to propagate over a shallow-water sloping region. This insight is used in many wave basins, where passive beaches are installed to promote dissipation and reduce reflections (Hughes, 1993; Tiedeman et al., 2012). According to Svendsen (1985), the optimum shape of such a dissipative beach is a parabola where the water depth h is described as:

$$h(x) = \frac{(x - x_{\mathrm{swl}})^2}{4gT_{\mathrm{des}}^2} \tag{4}$$

Here, x_{swl} is the location where the beach crosses the still water line and T_{des} is the design wave period for which the beach performs optimally. This parabolic beach shape is adopted for the top of the floater in the present study. However, the highest point of the floater is positioned below instead of right at the still water line (as discussed in next section). The equation that describes the parabolic top of the floater (z_{top}) is therefore modified to:

$$z_{\mathrm{top}}(x) = D_{\mathrm{f}} - \frac{(x + L_{\mathrm{f}}/2)^2}{4gT_{\mathrm{des}}^2} \tag{5}$$

Where D_{f} and L_{f} are the depth and length of the structure, respectively (see also Figure 1).

Based on insights from previous studies (Koutandos et al., 2004; Peña et al., 2011), it is anticipated that the breakwater length in direction of wave propagation should be of similar magnitude as the wave length in order to be effective. Therefore, the floater length L_{f} is much larger than its depth D_{f}. The floater has a flat bottom and is orientated such that the bottom in still water equilibrium is inclined at a slope of approximately $1 : 25$.

2.3 Submergence

The vertical position was selected such that the floater is sufficiently close to water surface to induce wave breaking, but at the same time, sufficiently far to ensure that the floater is continuously submerged. The latter constraint was considered essential because waterline crossings are expected to lead to high internal and local slamming loads.

The occurrence and location of depth-induced breaking is commonly predicted based on the wave height to water depth ratio at breaking (H_b/h_b), with extended empirical formulations accounting for, e.g., wave steepness and bed slope (Goda, 2010). For waves propagating over a submerged slope, a setting comparable to the submerged structure in the present study, Blenkinsopp and Chaplin (2008) found good agreement between experiments and the empirical prediction $H_b/h_b \geq 0.78$ for breaking occurrence. It is anticipated that in many applications of floating breakwaters, the main purpose is to reduce the highest waves in particular. Therefore, the draft in the experiment is chosen such that the empirical breaking criterion is exceeded for the highest tested waves whilst the lowest waves pass the floater without breaking.

2.4 Mooring design

Since the floater is fully submerged and has no hydrostatic stiffness, all stiffness originates from the mooring. It is foreseen that relatively high stiffness is required in especially the vertical direction, not only to avoid waterline crossings, but also to improve the attenuation performance (c.f., Loukogeorgaki and Angelides, 2005). The choice of mooring is highly site-specific, depending on wave conditions and water depth. A taut mooring is adopted in the present experimental study, but alternatives may be considered for other environmental conditions. Section 3.2.3 elaborates on the mooring lay-out for the present experiments.

3 Methods

3.1 Coordinate systems and sign convention

The present study uses a right-hand coordinate system. Distinction is made between global (earth-fixed) and local (model-fixed) coordinates. The origin of the local coordinate system x, y, z is at the intersect of mid-structure ($L_f/2$), centreline, and keel of the floater, the latter being defined as the bottom level at the floater's front side (Figure 1). The origin of the global coordinate system X, Y, Z is at the floater's mid-structure position, center-line basin, and water level in still-water equilibrium. Vertical coordinates are defined positive upward while the longitudinal coordinate X is defined positive against the direction of incident wave propagation.

Translational motions in X and Z directions are termed surge and heave, respectively. Rotational motions across the y axis are termed pitch (annotated θ) and are positive when the fore end (facing the waves) of the floater tilts downward. Loads in surge and heave directions are annotated F_x and F_z, respectively, while pitch moments are annotated M_y.

3.2 Model tests

3.2.1 Scaling

The experiments were performed at basin scale. The floater dimensions were selected to be in a realistic range given the dimensions of the basin and the wave conditions. In what follows, values will be reported in basin scale unless stated otherwise. For reference, as-built geometry values are also presented at prototype scale for a scale factor 15 (corresponding to inland lake conditions) and a scale factor 80 (corresponding to near-shore North Sea conditions), following Froude's law of similitude and assuming no differences in water density.

3.2.2 Floaters

Figure 2 shows photos of one of the floaters. Three floaters were engineered from solid wawa wood, reinforced with carbon fibre. The top of each model was milled to the desired parabolic shape, the sides and top of the

Figure 2: Photos of as-built model with grass cover, including instrumentation, in the same orientation as during the basin tests.

models were spray-painted. Only one of the floaters was tested in moored setup. This floater contained 24 bottom compartments that were filled with wooden and steel weights to calibrate the weight distribution. Prior to the basin tests, the weight distribution of the floater was measured using an oscillation table. The first bending mode of the floater had a natural frequency of 3.6 Hz (underwater), which exceeds the primary wave frequencies by a factor two to four. Hence, the measured motions during the tests in waves were governed by wave frequency excitation and response; oscillations at the floater's natural frequency only amounted to about 3% of the total variance of the the measured accelerations.

Table 1 presents the main geometric properties and measured weight distribution for the instrumented floater at basin and prototype scales. Note that the floater had a density $\rho_\mathrm{f} = 0.795$ kg/m^3, which is less than the water density $\rho_\mathrm{w} = 1000$ kg/m^3. Consequently, the floater has positive buoyancy, as also reflected in the negative values for the submerged weight w_f. During the tests, a vertically downward force is exerted by the mooring lines to realise the desired submerged position. Further, different draft values T_f are presented for the captive and moored setups, with the latter being 6% higher. This is explained by water absorption by the floater throughout the tests, resulting in a 5 kg increase in floater mass relative to weight measurements prior to testing that were used for designing and engineering the mooring lines. The mass properties in Table 1 are based on measurements directly after the moored setup tests.

For some of the tests, the top of the tested floater (model 2 in Figure 3) was covered with a layer of artificial grass. The aim of this grass cover was to simulate the effects of additional roughness, reflecting possible secondary ecological purposes of the floater such as a shellfish or vegetated cover. The grass cover was selected from stock materials to have a surface roughness in a similar roughness regime as prototype shellfish or vegetation covers. The polypropylene grass cover had a height of 8 mm (model scale), was uniformly distributed, and fairly stiff. For the wave conditions tested, the floater with roughness layer would classify as hydraulically 'very rough' following Jonsson (1980) at model as well as prototype scale. Assuming a roughness height k_s equal to the height of the grass stems, the apparent roughness at prototype scale equals $z_0 = k_\mathrm{s}/30 = 4$, mm which is about half the value for oyster beds (Wright et al., 1990). The grass cover was practically neutrally buoyant, as also follows from Table 1 which shows that the submerged weight of the roughness layer is very small compared to the total weight of the floater.

Table 1: As-built model geometry, weight distribution, and mooring specifications. Values are provided at model scale and at prototype scale for scale factor 15 (corresponding to an inland lake) and scale factor 80 (corresponding to near-shore conditions) following Froude's law of similitude.

Designation	Symbol	Model scale	Proto (1:15)	Proto (1:80)	unit
Floater geometry and weight distribution:					
Length	L_f	1.135	17.02	90.8	[m]
Width	W_f	3.401	51.01	272.1	[m]
Depth	D_f	0.083	1.24	6.6	[m]
Thickness	t_f	0.033	0.5	2.7	[m]
Draft captive setup	T_f	0.176	2.64	14.1	[m]
Draft moored setup	T_f	0.187	2.80	14.9	[m]
Water depth above top floater	h_0	0.093	1.40	7.47	[m]
Parabolic shape parameter	T_{des}	0.852	3.30	7.62	[s]
Displacement volume	V_f	175	$590 \cdot 10^3$	$90 \cdot 10^6$	[m^3]
Mass floater	m_f	139	$470 \cdot 10^3$	$71 \cdot 10^6$	[kg]
Submerged weight	w_f	-351	$-1.19 \cdot 10^6$	$-180 \cdot 10^6$	[N]
Density	ρ_f	0.795	0.795	0.795	[kg/m^3]
Height roughness elements	k_s	0.008	0.12	0.64	[m]
Submerged weight roughness layer	w_{rl}	-0.35	$-1.2 \cdot 10^3$	$-0.18 \cdot 10^6$	[N]
Longitudinal center of buoyancy	x_{cb}	0	0	0	[m]
Vertical center of buoyancy	z_{cb}	0.045	0.68	3.63	[m]
Longitudinal center of gravity	x_{cg}	0	0	0	[m]
Vertical center of gravity	z_{cg}	0.055	0.82	4.37	[m]
Roll radius of gyration	k_{xx}	1.026	15.39	82.1	[m]
Pitch radius of gyration	k_{yy}	0.317	4.76	25.4	[m]
Yaw radius of gyration	k_{zz}	1.068	16.02	85.4	[m]
Mooring:					
Unstretched line length	l	0.58	8.7	46.4	[m]
Axial stiffness	AE	783	$2643 \cdot 10^3$	$401 \cdot 10^6$	[N]
Pretension	$F_{T,0}$	66.7	$225 \cdot 10^3$	$34 \cdot 10^6$	[N]
Strain	$F_{T,0}/AE$	8.5	8.5	8.5	[%]
Submerged weight	W_{subm}	4.6	$1.03 \cdot 10^3$	$29.4 \cdot 10^3$	[N/m]
Angle w.r.t. vertical in still water	α	45.7	45.7	45.7	[deg]
Surge stiffness	k_{11}	858	$193 \cdot 10^3$	$5.5 \cdot 10^6$	[N/m]
Heave stiffness	k_{33}	$5.5 \cdot 10^3$	$1.2 \cdot 10^6$	$35 \cdot 10^6$	[N/m]
Pitch stiffness	k_{55}	$1.7 \cdot 10^3$	$84 \cdot 10^6$	$68 \cdot 10^9$	[Nm/rad]
Surge-heave coupling term	k_{31}	37	$8.4 \cdot 10^3$	$239 \cdot 10^3$	[N/m]
Surge-pitch coupling term	k_{51}	-25	$-84 \cdot 10^3$	$-13 \cdot 10^6$	[N/rad]
Heave-pitch coupling term	k_{53}	179	$604 \cdot 10^3$	$92 \cdot 10^6$	[N/rad]

3.2.3 Mooring layout

The mooring designed for the present experiments was subject to a number of constraints. Firstly, the mooring should result in large stiffness in order to promote the breakwater's effectiveness and prevent high slamming loads due to waterline crossings (see also Section 2.4). At the same time, the natural frequencies of the floating breakwater should be well outside the wave frequent regions in order to prevent resonant motion behaviour in waves and, accordingly, limit peak mooring line loads. Finally, slack lines, leading to snap loads, and unrealistically high line tensions, leading to line failure at prototype scale, should be avoided.

Because only normal-incident waves were tested, the roll, sway and yaw degrees of stiffness were disregarded and the mooring design focused on the performance in terms of surge, heave, and pitch motions. Using the mass and added mass properties (latter obtained from linear diffraction software, see Section 3.3), the mooring was designed to match the above constraints for the selected water depth and wave conditions. This procedure resulted in a mooring layout involving eight lines, connected to bottom anchors at the same X but different Y position as the connections at the floater (see Figure 3). In still water conditions, the line angle in the $Y - Z$ plane is approximately 45 deg (Figure 3c). Each line consisted of a steel wire and a linear spring segment. Table

1 presents the mean properties of the mooring lines. The stiffness terms were calculated based on mooring line properties and line connection coordinates, and were verified through static load tests prior to testing.

3.2.4   Basin setup and instrumentation

The experiments were performed in the Shallow Water Basin at the Maritime Research Institute Netherlands (MARIN). This basin is 220 m long, 15.8 m wide, and tests were performed at a water depth of $h = 0.667$ m. The basin is equipped with piston-type wave makers at one end and passive absorbing beaches at the other end. A measurement carriage spans the width of the basin.

The setup of the models, mooring lines, and wave gauges is shown in Figure 3. To reduce asymmetries in the wave field, three models were positioned in the basin. The outer two models were positioned at legs on the basin floor and were not instrumented. The centre model was first tested in a captive setup, with the model connected through a six-component force frame to the basin carriage, and later in a moored setup, with the model moored through eight lines to anchor points on the basin floor. The distance from the centre of the models to the wave maker was $\Delta X = 25.0$ m.

Note that the water absorption (see Section 3.2.2) occurred predominantly throughout the tests in captive setup, during which the floater was completely submerged for more than four days. For the tests in moored setup, a 1 mm difference in floater draft in still water equilibrium was observed between the start and the completion of the tests. This difference is considered within the range of measurement uncertainty and it indicates that the floater draft was stable throughout the tests in moored setup.
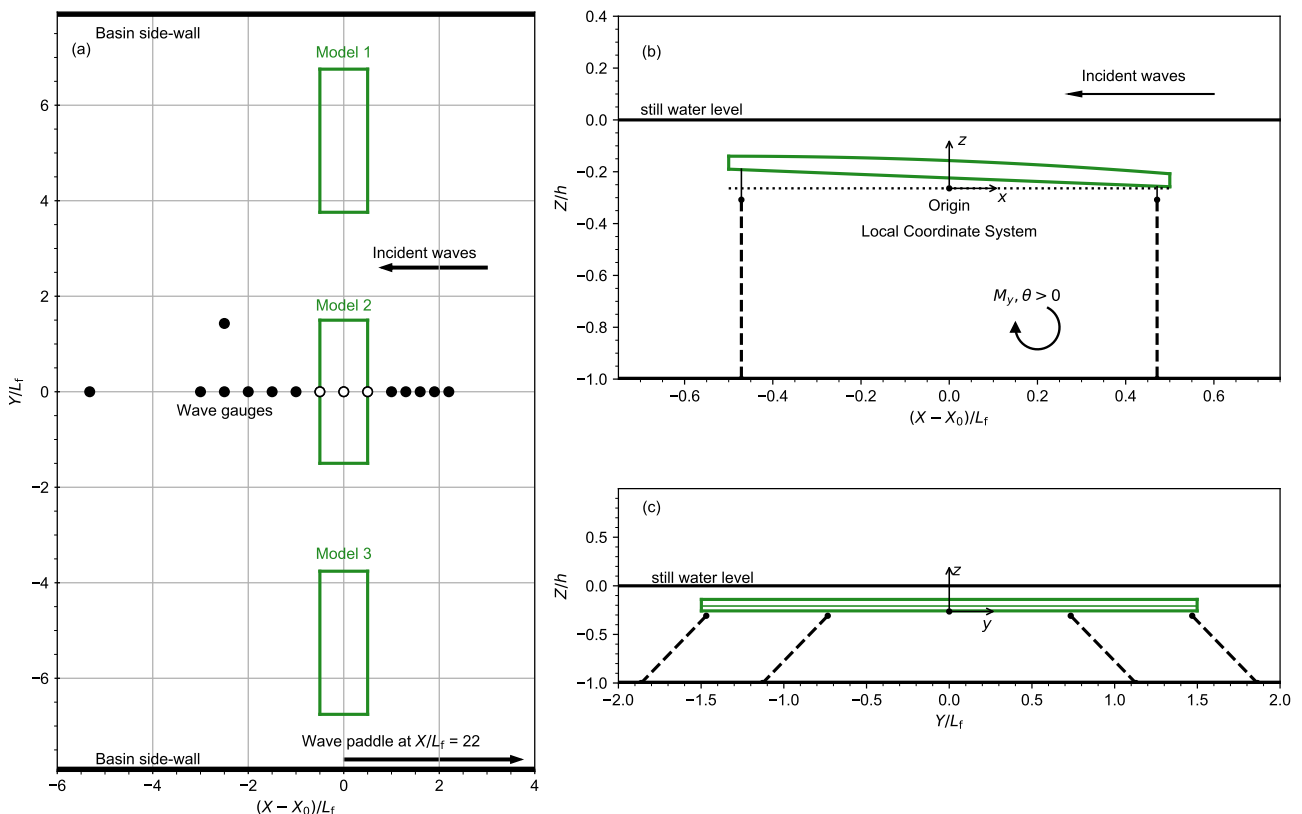

Figure 3: Basin setup. (a) Top view, showing locations of the three models and of the resistive (black circles) and acoustic (white circles) wave gauges; (b) Side view of center floater, including origin of the local coordinate system and mooring lines (dashed); (c) front view of center floater including mooring lines (dashed). Horizontal and vertical axes have been normalised by floater length L_f and water depth h, respectively, whilst respecting the aspect ratios of the actual geometry.

Twelve resistive and three acoustic wave gauges were deployed during the model tests in waves. The locations of these wave gauges are indicated in Figure 3a. Most wave gauges were deployed along the centreline of the

basin in order to measure the wave field in front and at lee side of the middle breakwater. Prior to the tests in waves, the undisturbed waves were measured at the centre location of the model ($X = 0$, $Y = 0$) without any models in the basin.

During the tests in moored setup the motions of the floater were measured using a Northern Digital optical tracking system. The motion target on the floater can be seen in Figure 2. The floater was further instrumented with accelerometers, used primarily for verification of the motion measurements. Each mooring line was instrumented with a tension ring at the connection point to the floater.

3.2.5   Environmental conditions

The floating breakwater was tested in a range of regular and irregular wave conditions. An overview of the measured undisturbed wave conditions is presented in Table 2. Regular wave heights H were calculated as twice the measured amplitude of the first harmonic component ($H = 2a_i$); significant wave heights were calculated as $H_s = 4\sigma(\eta)$, with $\sigma(\eta)$ representing the standard deviation of the water surface elevation η. The presented wave lengths are based on linear wave theory for water depth $h = 0.667$ m and are for the irregular waves based on the peak period T_p. Note that conditions REG06 and REG11 correspond to waves at intermediate water depth ($h/L_{\text{wave}} < 0.5$) while the other conditions can be considered deep water waves.

Table 2: Overview of wave conditions: measured values during wave calibration at centre position of the model.

Name	Type	$H_{(s)}$ [m]	$T_{(p)}$ [s]	L_{wave} [m]	$H_{(s)}/L_{\text{wave}}$	$H_{(s)}/h_0$	L_f/L_{wave}
REG01	Regular	0.059	0.66	0.68	0.087	0.63	1.68
REG02	Regular	0.057	0.71	0.79	0.072	0.61	1.44
REG03	Regular	0.060	0.77	0.94	0.064	0.64	1.21
REG04	Regular	0.057	0.85	1.13	0.050	0.61	1.00
REG05	Regular	0.057	0.93	1.34	0.042	0.61	0.84
REG06	Regular	0.059	1.06	1.72	0.034	0.64	0.66
REG07	Regular	0.069	0.71	0.79	0.088	0.74	1.44
REG08	Regular	0.087	0.77	0.94	0.093	0.93	1.21
REG09	Regular	0.100	0.85	1.13	0.088	1.07	1.00
REG10	Regular	0.117	0.93	1.34	0.087	1.26	0.84
REG11	Regular	0.160	1.06	1.72	0.093	1.73	0.66
WN	White noise	0.027	0.5 - 1.8	-	-	-	-
JONS01	JONSWAP	0.038	0.85	1.14	0.033	0.41	1.00
JONS02	JONSWAP	0.047	0.88	1.21	0.039	0.50	0.94
JONS03	JONSWAP	0.056	0.85	1.14	0.049	0.60	1.00
JONS04	JONSWAP	0.082	1.05	1.71	0.048	0.89	0.66

A total of 11 regular (monochromatic) waves were used. Conditions REG01 to REG06 have similar wave height $H \approx 0.058$ m but varying wave period T. This wave height was selected such that waves were expected not to break upon interaction with the breakwater. This also follows from the parameter H/h_0, which represents the relative wave height of the undisturbed wave over the minimum water depth above the floater. Empirical criteria for onset of wave breaking predict that waves with $H/h_0 < 0.7$ will not break (Blenkinsopp and Chaplin, 2008; Goda, 2010). Conditions REG01 and REG07 to REG11 were selected to cover different periods with similar wave steepness ($H/L_{\text{wave}} \approx 0.09$). From these conditions, especially the longer-period, higher waves were expected to break over the floater.

Further, a total of five long-crested irregular sea states were tested. Figure 4 presents the measured spectra for these conditions. The irregular conditions include firstly a white noise condition with a low energy content that is distributed uniformly across wave periods in the range of 0.5 to 1.8 s. This condition is mainly used to study the breakwater's motion response in a regime with approximately linear waves. Further, four JONSWAP waves with peak enhancement factor $\gamma = 3.3$ were tested. Conditions JONS01 to JONS03 have same peak period T_p but increasing H_s. Condition JONS04 has higher T_p and H_s but similar wave steepness, based on waves with wave height H_s and period T_p, as condition JONS03.
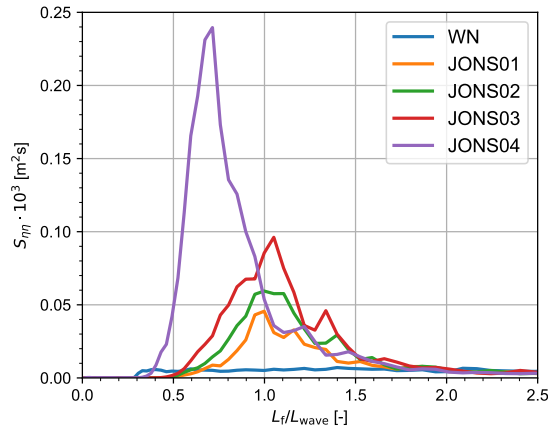
Figure 4: Calibrated irregular wave conditions at centre location of the model.

3.2.6 Experimental procedures

All wave gauges were calibrated prior to the tests by moving them vertically over a set distance. The line load transducers were calibrated in the workshop and were zeroed out at the start of each test day to correct for any signal drifts due to temperature differences; the pretension was added in the post-processing of results. The optical measurement system was referenced through a measurement with the breakwater at known location in captive setup.

After connecting the mooring lines, pitch and roll angles were calibrated to < 1 deg by adjusting the pre-tensions in the lines. The mooring stiffness was verified through static load tests in surge, heave, and pitch directions. In addition, motion decays were performed in surge and pitch directions by measuring the floater's return to equilibrium following an initial offset. Surge decays were performed both with and without the top roughness layer.

The test duration was five minutes for the regular wave tests and twelve minutes for the irregular wave tests. A waiting time of at least ten minutes in between tests was ensured.

3.2.7 Data treatment

In the post-processing, the measured positions were translated to the centre of gravity (CoG) of the floater. For verification, positions were also obtained through double integration of the accelerometers, showing excellent agreement with the optical position measurements. The measured line loads and floater positions were combined to derive the total mooring loads on the floater.

For all conditions, waves established a quasi-equilibrium state after a ramp-up period of approximately one minute. Statistics were calculated over 20 wave cycles for the regular wave tests and over 10 minutes of data for the irregular wave tests, following this ramp-up period. For both regular and irregular wave conditions, first-order response amplitude operators (RAOs) were calculated for loads, motions, and water surface levels as the measured amplitude of each variable over the amplitude of the undisturbed incident wave. Second-order quadratic transfer functions (QTFs; main diagonal) were calculated for the regular-wave tests only by dividing the measured mean force (surge, heave, pitch directions) over the squared amplitude of the undisturbed incident wave.

For the regular waves, amplitudes of the measured waves in front of the floater were decomposed into an incident component a_i and a reflected component a_r, by applying the wave splitting methodology of Goda and Suzuki (1976) to the wave gauges at fore side of the floater (see Figure 3). Note that this methodology applies to the primary harmonic component of the incident and reflected waves. The wave reflection coefficient was then calculated as $K_r = a_r/a_i$. The transmission coefficient for the regular wave tests was calculated through $K_t = a_t/a_i$ using, analogous to K_r, the first harmonic of the transmitted wave (a_t). Following conservation of energy, it follows that (e.g., Ji et al., 2016)

$$K_r^2 + K_t^2 + K_l^2 = 1 \tag{6}$$

where K_l is a loss coefficient. Using K_r and K_t, the loss coefficient was quantified by resolving Eq. 6. Note that because the tests were three-dimensional, K_l does not only represent the energy that is dissipated but also the wave energy that is diffracted and radiated to other directions than the lee side of the breakwater.

3.3   Wave diffraction calculations

The experimental results were complemented by linear wave diffraction and radiation calculations using the program DIFFRAC. The program solves the linearized velocity potential over a structure's geometry, represented by a large number of source panels. The frequency-dependent pressure distribution over the structure is integrated to yield the total wave loads, added mass, and damping. The program assumes infinitesimal wave amplitudes and does not account for nonlinear effect such as wave breaking. Motion RAOs are obtained by combining the linear wave exciting forces, added mass, damping values, and a linear mooring stiffness matrix. More background on the applied wave diffraction theory can be found in, e.g., Buchner et al. (2001), Buchner (2006), and Pauw et al. (2007).

The diffraction calculations in the present study were performed using a panel distribution of the as-built geometry, with weight and mooring stiffness properties as specified in Table 1 and using the same water depth $h = 10$ m as during the basin tests. The applied total hydrodynamic damping values were adopted from the motion decay test results. The calculations were performed for a single stand-alone floater as well as for a multi-body setup of three longitudinally separated floaters with same positioning as during the basin tests. In the latter calculations, consistent with the basin tests, the outer floaters were kept captive while the center floater was either captive or moored.

The diffraction calculations do not consider nonlinear processes, such as wave breaking, which are relevant for the present breakwater's behaviour and performance. Therefore, the analyses in the upcoming results sections focus primarily on the wave basin tests. The diffraction calculations are primarily performed for verification purpose and to shed additional insights into the wave field around the structure. In addition, the single-body and multi-body calculation results are compared to assess the effect of hydrodynamic interactions between the floaters during the basin tests.

4   Motions and damping of moored floating breakwater

4.1   Natural periods and damping

Prior to the tests in waves, motion decays were performed in surge and pitch directions (see Section 3.2.6). Natural periods and damping coefficients were established by fitting a second-order polynomial through the crests and troughs of the measured motion signal. Table 3 presents the natural periods T_n and linearised damping coefficients B_{lin} (as percentage of the critical damping). The latter values were calculated for two amplitudes that are within the typical range of motions during the irregular wave tests ($0.05L_f$ and $0.1L_f$ for surge; 1 and 2 deg for pitch). To facilitate comparisons with wave conditions at later stage, natural periods are also represented in non-dimensional form through $L_f/L_{wave,n}$, where $L_{wave,n}$ is the theoretical wave length of a wave with $T = T_n$ for the water depth h in the basin following linear (Airy) wave theory.

The natural surge and pitch periods are in the range of 2 to 3 s. As explained in Section 3.2.3, these natural periods were designed to be just above the periods of wave excitation. The comparison of surge decays with and without grass cover shows that the roughness layer increases the natural period by 10%. This corresponds to an increase in the combined mass and added mass (i.e., the added system inertia due to water displacement when the floater moves) by 22%. Because the roughness layer itself is practically neutrally buoyant, the change in natural periods is fully attributed to an increase in added mass.

Linearised damping values are in the range of 6 to 14%. For surge motions without grass cover, both surge amplitudes yield similar B_{lin}, indicating that the damping is predominantly linear. With grass cover, the damping values increase considerably, likely due to the enhanced viscous dissipation by the rougher surface. Furthermore, B_{lin} values increase with surge amplitude, indicating a significant quadratic damping contribution. The latter is also observed for the damping coefficients in pitch direction.

The setup in the basin did not allow clean decays in heave direction. However, during the surge and pitch decays a small offset in heave was also introduced, allowing quantification of the natural heave period at

$T_\mathrm{n} = 6.70$ s for setups both with and without roughness.

Table 3: Natural periods and damping values at model scale.

Description	T_n [s]	$L_\mathrm{f}//L_\mathrm{wave,n}$	B_lin at $0.05L_\mathrm{f}$ [%]	B_lin at $0.10L_\mathrm{f}$ [%]
Surge (without grass cover)	2.71	0.174	7.7	6.6
Surge (with grass cover)	3.00	0.156	9.0	13.6
Heave (without grass cover)	6.70	0.067	-	-
Heave (with grass cover)	6.70	0.067	-	-

Description	T_n [s]	$L_\mathrm{f}/L_\mathrm{wave,n}$	B_lin at 2 deg [%]	B_lin at 4 deg [%]
Pitch (with grass cover)	2.36	0.19	9.7	14.0

4.2 Motions in waves

The present section describes the breakwater's motions in waves. For brevity, results are limited to the irregular wave tests.

Figure 5a-c present the measured spectra of the floater motions in three degrees of freedom in irregular waves. Each panel shows energy in the short-wave frequency regions ($L_\mathrm{f}/L_\mathrm{wave} = 0.5$ to 1.2) and in the low frequency regions (around $L_\mathrm{f}/L_\mathrm{wave} = 0.1$). The latter peaks are due to fluctuations at the natural frequency of the breakwater, excited by fluctuating second-order wave drift loads. In surge and heave directions, the floater moves predominantly at its natural frequency (Figure 5a-b), whilst pitch motions are dominant at wave frequencies (Figure 5c). The low-frequency peaks in spectral energy are found at $L_\mathrm{f}/L_\mathrm{wave} = 0.17$ (surge), 0.08 (heave), and 0.21 (pitch). These values are slightly higher than $L_\mathrm{f}/L_\mathrm{wave,n}$ based on the natural periods (see previous section). This is attributed to the floater offset compared to still water equilibrium due to net drift loads, resulting in an increase in mooring stiffness.

The motion spectra show large differences in energy from condition WN to JONS04, which is largely explained by differences in incident wave energy. Figure 5d-f present the motion RAOs, i.e., the linear response amplitude over the incident undisturbed wave amplitude. In this representation, all wave conditions produce a similar response. This shows that the motion response does not depend significantly on the amplitude of the incident wave, i.e., the response is largely linear. An exception is the pitch response for $L_\mathrm{f}/L_\mathrm{wave} = 0.5$ to 1.0, which shows a progressively lower pitch RAO with increasing H_s (JONS01 to JONS04). This relates to quadratic damping contributions (see Table 3), possibly aided by intensifying wave shoaling and breaking over the breakwater with increasing H_s.

For reference, Figure 5d-f includes the motion RAOs following linear wave diffraction calculations through a single-body (solid grey line) and a multi-body (dashed black line) approach, with the latter matching the basin setup. By exception of the heave response for $L_\mathrm{f}/L_\mathrm{wave} < 0.6$ (Figure 5e), both numerical approaches lead to nearly identical results, which indicates that any hydrodynamic interactions between the three floaters in the basin have minor effect on the motion response.

The figure further shows that the calculated motion RAOs are qualitatively similar to the measurements, although notable differences are observed. For heave and pitch motions (Figure 5e-f), the magnitudes of the measured RAOs are smaller than the numerical results. This is attributed to an overestimation in calculated wave amplitude around and above the structure and is most apparent for the pitch response, which shows larger differences between numerical and experimental results with increasing wave height (JONS01 to JONS04). The measured heave response at $L_\mathrm{f}/L_\mathrm{wave} < 0.6$ shows a better agreement with the multi-body than the single-body numerical calculations (Figure 5e), which indicates that the multi-body diffraction calculations adequately capture the hydrodynamic interaction between the floaters. In surge (Figure 5d), the diffraction calculations show a shift in RAO towards lower $L_\mathrm{f}/L_\mathrm{wave}$, possibly due to nonlinear dispersion processes in the experiments leading to shorter wave lengths around the structure compared to the calculations.

Note that the diffraction calculations assume infinitesimal, linear waves, whilst the actual waves are expected to behave strongly nonlinearly around and above the structure. In addition, a fully linear and constant (i.e., no dependency on offset position) mooring stiffness is assumed. These factors explain the main differences between calculated and measured motion RAOs. In what follows, the primary purpose of the diffraction results is to complement the measurements and shed qualitative insights into the diffracted and radiated wave field. For

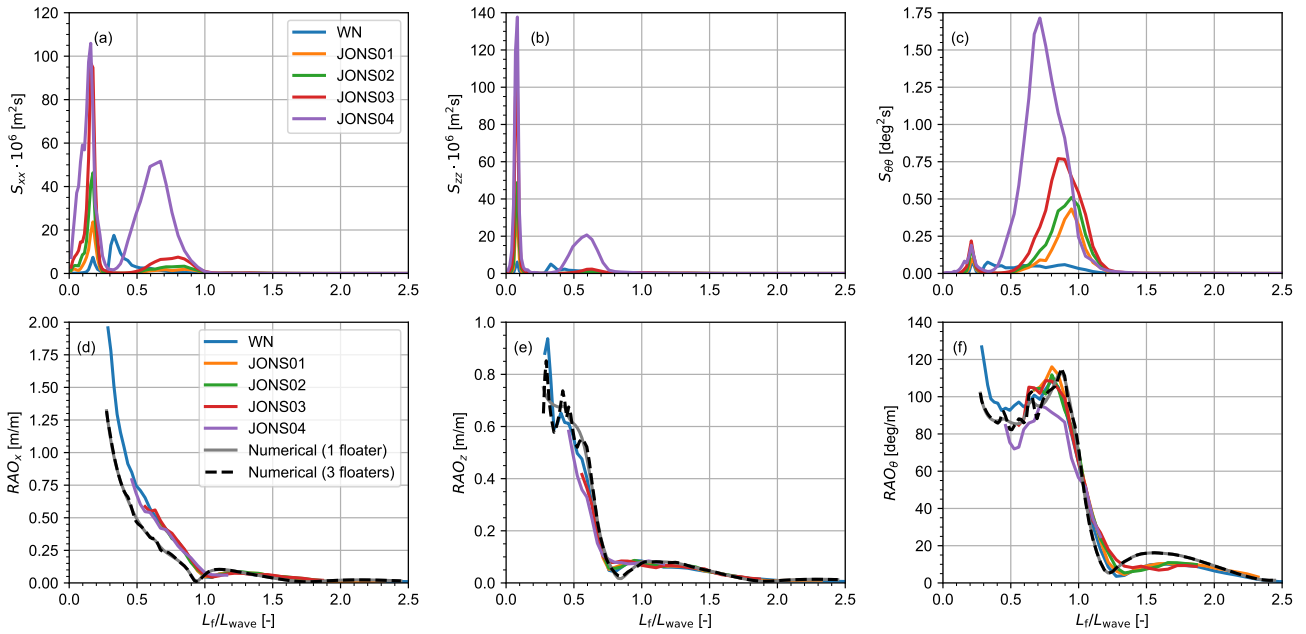this purpose the numerical results are considered acceptable.

Figure 5: Spectra (top panels) and RAOs (bottom panels) of floater motions in surge (left), heave (mid), and pitch (right) directions for five irregular wave conditions in basin tests (coloured solid lines). The RAOs include the results of linear wave diffraction calculations for a single floater (solid grey) and for the center model of three longitudinally separated floaters (black dashed). All tests featured the grass cover on the floater.

During the experiments, tests were performed with and without grass cover on top of the floater. The effect of the roughness layer is assessed through Figure 6, which presents the motion spectra for two wave conditions. Without roughness layer (dashed lines), a larger motion response is measured in all degrees of freedom, most apparently for condition JONS04. Removal of the roughness layer also shifts the peak in low-frequency surge response towards higher frequency (i.e., higher L_f/L_{wave}). Both these observations (lower damping and higher T_n without grass cover) are consistent with the motion decay results (Section 4.1). These results show that the addition of a surface roughness layer to the floater can considerably reduce motions.
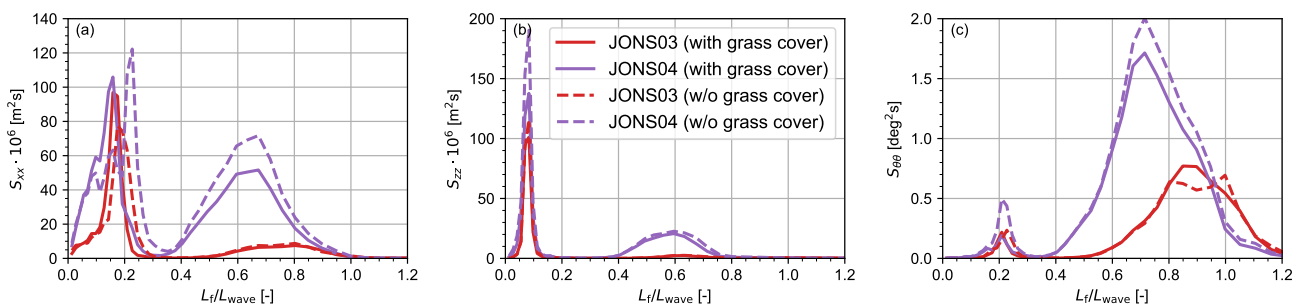

Figure 6: Spectra of floater motions in surge (a), heave (b), and pitch (c) directions for JONS03 (red) and JONS04 (purple), with (solid) and without (dashed) grass cover.

5 Wave attenuation performance

The present section presents the wave attenuation performance of the floating breakwater for the regular wave (Section 5.1) and irregular wave (Section 5.2) conditions for the captive and the moored setups.

5.1 Regular waves

5.1.1 Spatial variability of wave field

Figure 7 explores the water surface elevations for two captive setup tests with similar T but different H (REG06 and REG11). Visually it was observed that the waves for condition REG06 passed the breakwater without breaking, while plunging-type breaking was observed for the REG11 waves.

Figure 7a-c presents time series of the water surface at three different locations, i.e., upwave of the floater (panel a), above the aft side of the floater (panel b), and at lee side of the floater (panel c). For condition REG06 (black line), the waves are approximately linear at upwave location, become highly nonlinear above the floater, and return to an approximately linear shape at lee side of the breakwater. The waves have similar amplitude at upwave and downwave locations of the structure, which implies that most wave energy is transmitted (i.e., $K_t \approx 1$). The wave evolution shows a strong resemblance to the experimental observations by Beji and Battjes (1993) for shoaling and de-shoaling non-breaking waves that propagate over a bar. The wave phase was presented such that both conditions have the same phase at $X/L_f = 1.94$. The results in Figure 7b-c show a difference in relative phase between both conditions, indicating nonlinear wave propagation speed (amplitude dispersion) over the structure.

At the shown upwave location (Figure 7a) waves are approximately linear and have notably high amplitudes ($a/a_i \approx 1.2$ for REG06 and $a/a_i \approx 2$ for REG11). This is explained by wave reflection on the floater, resulting in a standing wave pattern upwave of the floater with the present location being close to an anti-node. The higher normalized amplitudes for condition REG11 compared to REG06 indicate a higher reflection coefficient for the former condition (see also Section 5.1.2).

Above the floater, waves are strongly nonlinear and display considerable wave-to-wave variability due to the waves being at onset of breaking (Figure 7b). At lee side of the floater (Figure 7c), the REG11 waves have reduced considerably in amplitude (i.e., $K_t < 1$) due to wave energy being reflected, diffracted, and dissipated.
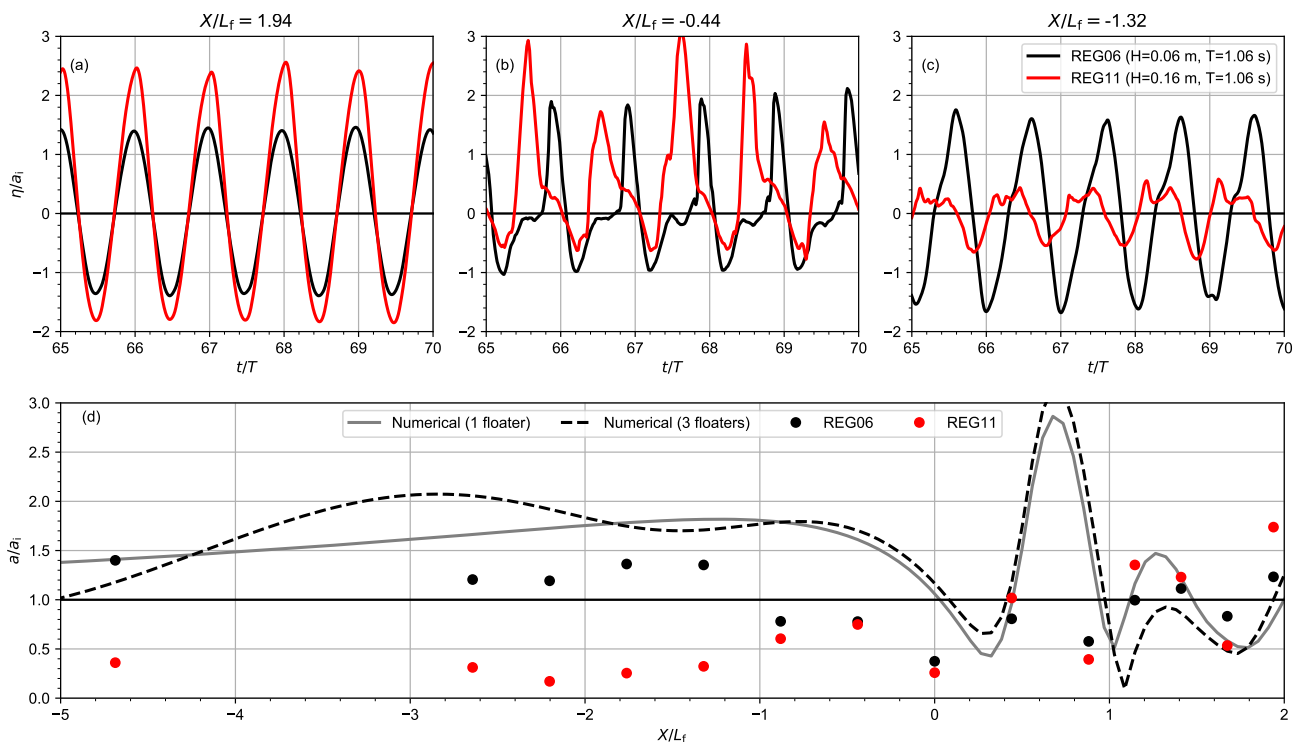

Figure 7: Time series and amplitudes of water surface level for wave conditions REG06 and REG11 in captive setup. (a-c) Time series at three selected locations; (d) Wave amplitude over incident amplitude at various X positions along the centerline of the basin: measurements (circles) and diffraction calculations for a single-body (solid grey line) and a multi-body (dashed line) setup.

The spatial variability of the wave field is further explored through Figure 7d, which shows the measured

normalized wave amplitude a/a_i as function of longitudinal distance X. Results of linear wave diffraction calculations are added here for reference.

At $0.5 < X/L_f < 2$, measured amplitudes for both conditions fluctuate around the incident wave amplitude ($a/a_i = 1$). The fluctuations are explained by a standing wave pattern resulting from incident waves and reflected waves travelling in opposite directions. Nodes and anti-nodes of the standing wave are observed at similar X positions for both wave conditions, with larger spatial fluctuations of a/a_i for condition REG11 implying a higher reflection coefficient. Wave heights at lee side of the breakwater ($X/L_f < -0.5$) have reduced for condition REG11 ($a/a_i < 1$), implying wave attenuation due to a combination of wave reflection and dissipation. However, waves for condition REG06 show an enhanced wave amplitude ($a/a_i > 1$) at lee side. These differences between wave conditions are further explored in Section 5.1.2.

The single-body and multi-body linear diffraction calculations lead to similar results for $-2 < X/L_f < 1$, but differ at larger offset distances due to a more complicated diffraction pattern for the multi-body calculations. The multi-body numerical results (dashed line in Figure 7d) yield wave amplitudes which upwave of the floater ($X/L_f > 0$) are similar to the measurements for condition REG06 (non-breaking waves). However, amplitudes at lee side of the breakwater ($X/L_f < 0$) are overestimated, possibly due to the neglecting of viscous losses, energy transfer to higher harmonics, and other nonlinear processes. Consistent with the measurements for non-breaking waves, the diffraction calculations predict $a/a_i > 1$ at lee side of the breakwater. Such enhanced wave amplitudes are not expected for a 2D setup of the floating breakwater and are therefore attributed to 3D diffraction around the structure.
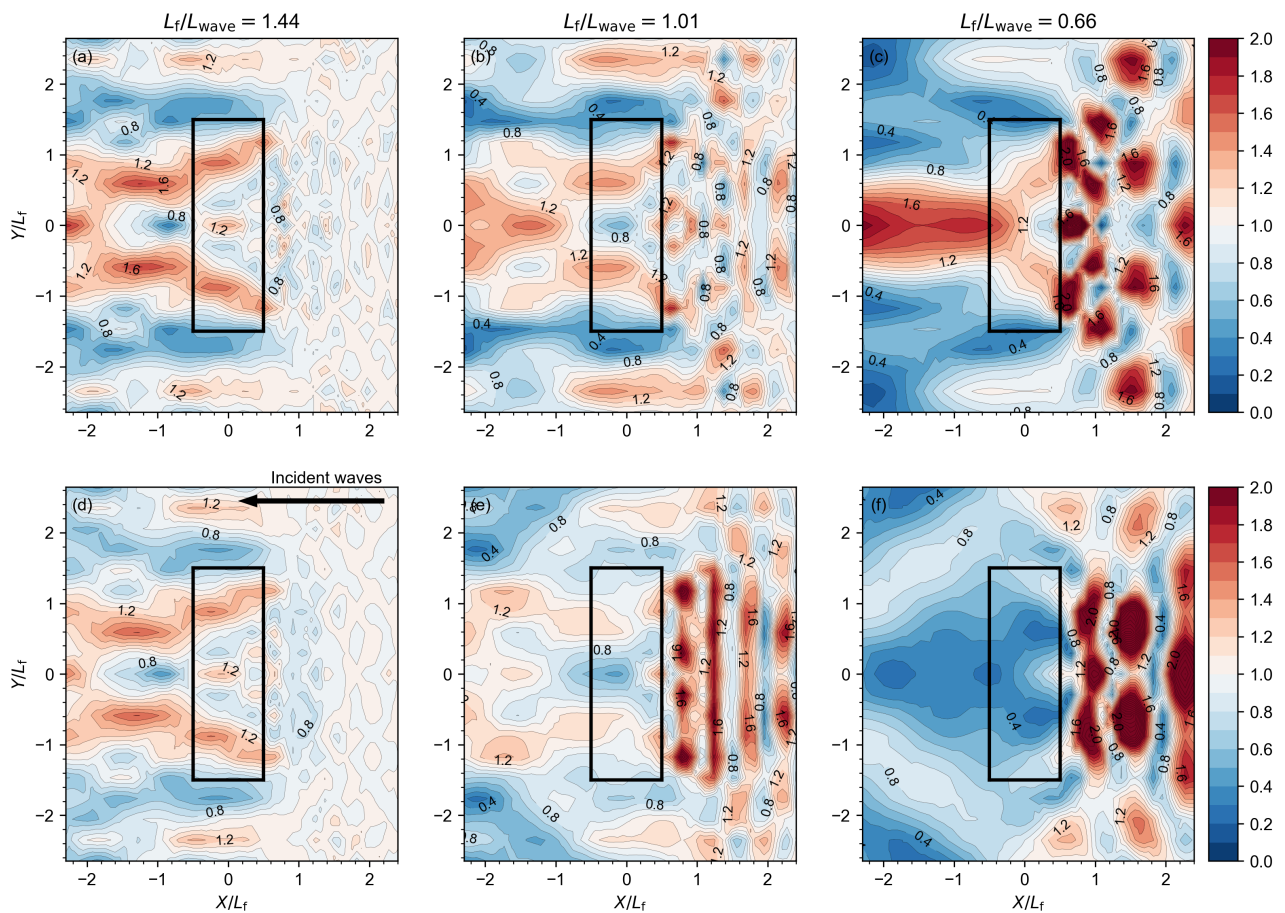

Figure 8: Colour contour plots of the spatially varying normalized wave amplitude a/a_i following linear wave diffraction calculations for three wave periods (left to right) in captive setup (a-c) and moored setup (d-f). The solid line marks the contour of the floater in still water conditions.

These 3D effects are further explored through Figure 8, which shows the spatial contour of the normalized wave amplitude for different wave conditions and both test setups according to the multi-body linear wave

diffraction calculations. The wave field shown is the result of wave incidence, reflection, diffraction, and (for moored setup) radiation. For all wave conditions, a highly nonuniform wave field is observed. Several conditions result in enhanced wave amplitudes along centerline and at lee side of the breakwater ($X/L_\mathrm{f} < 0$, $Y/L_\mathrm{f} = 0$) as a result of 3D wave diffraction.

The diffraction calculations do not account for viscous losses due to friction and breaking and as such, cannot be used to establish reliable transmission coefficients for all wave conditions. Therefore, transmission, reflection and loss coefficients in what follows are based on the wave measurements during the basin tests. It is noted that the restricted number of wave measurements in combination with the non-uniform wave field results in considerable uncertainty in the established coefficients. This uncertainty was reduced by calculating K_t as the average of the three wave gauges closest to the breakwater, which were overall (for all wave conditions) the most uniform. Furthermore, the analysis will focus primarily on comparison between wave types (breaking versus non-breaking) and setups (captive versus moored) within the present tests, with limited comparison against earlier (2D) studies.

5.1.2   Wave transmission for captive setup

Table 4 presents a summary of the main results for the regular wave tests. The reflection, transmission, and loss coefficients are discussed in the present sections; the quadratic transfer function (QTF) values are addressed in Section 6.

For the captive setup tests, waves REG02 to REG06 propagate over the breakwater without breaking (Table 4). The other wave conditions break over the structure, with an increased intensity of breaking (from spilling to plunging) for increasing wave period and wave height. Transmission (K_t), reflection (K_r), and loss (K_l) coefficients vary considerably between wave conditions. Wave conditions REG05 and REG06 result in $K_\mathrm{t} > 1$ and $K_\mathrm{l} < 0$, which is not physical and attributed to the uncertainty in K_t due to spatial variability effects as discussed in the previous section.

Table 4: Summary of regular wave results: classification of wave breaking type; wave reflection, transmission, and loss coefficients; and quadratic transfer functions in surge, heave, and pitch directions.

Wave condition	H/h_0 [-]	$L_\mathrm{f}/L_\mathrm{wave}$ [-]	Breaking type	K_t [-]	K_r [-]	K_l [-]	QTF_x [kN/m^2]	QTF_z [kN/m^2]	QTF_θ [Nm/m^2]
			Captive setup:						
REG01	0.63	1.68	Spilling	0.44	0.30	0.85	-0.98	44.7	170
REG02	0.61	1.44	Non-breaking	0.83	0.19	0.52	-1.62	30.0	121
REG03	0.64	1.21	Non-breaking	0.66	0.49	0.57	-4.35	23.0	132
REG04	0.61	1.00	Non-breaking	0.64	0.53	0.55	-5.46	21.0	151
REG05	0.61	0.84	Non-breaking	1.09	0.43	-0.61	-0.67	43.4	127
REG06	0.64	0.66	Non-breaking	1.17	0.22	-0.64	-0.55	47.5	134
REG07	0.74	1.44	Spilling	0.66	0.13	0.74	0.48	36.1	108
REG08	0.93	1.21	Weakly plunging	0.68	0.09	0.73	0.84	26.6	64
REG09	1.07	1.00	Weakly plunging	0.79	0.28	0.55	-0.36	22.0	55
REG10	1.26	0.84	Plunging	0.79	0.39	0.47	-1.12	22.8	36
REG11	1.73	0.66	Plunging	0.39	0.52	0.76	-2.67	16.1	24
			Moored setup:						
REG01	0.63	1.68	Non-breaking	0.72	0.29	0.63	-3.12	26.2	168
REG02	0.61	1.44	Non-breaking	0.73	0.08	0.68	-1.19	22.1	118
REG03	0.64	1.21	Non-breaking	0.79	0.04	0.61	-1.04	20.8	112
REG04	0.61	1.00	Non-breaking	0.57	0.39	0.72	-4.92	23.9	151
REG05	0.61	0.84	Non-breaking	0.28	0.67	0.69	-15.27	20.4	188
REG06	0.64	0.66	Non-breaking	0.33	0.65	0.69	-13.34	21.5	68
REG07	0.74	1.44	Spilling	0.56	0.12	0.82	-0.60	33.1	107
REG08	0.93	1.21	Spilling	0.55	0.09	0.83	-0.31	23.7	58
REG09	1.07	1.00	Weakly plunging	0.69	0.11	0.72	-1.45	16.5	43
REG10	1.26	0.84	Plunging	0.64	0.19	0.74	-4.88	18.9	35
REG11	1.73	0.66	Plunging	0.53	0.45	0.72	-7.61	20.2	30

The coefficients for captive setup are further explored through Figure 9a,c,e. Figure 9a shows the transmission coefficients; the whiskers indicate the relatively high uncertainty in the K_t estimates. The non-breaking waves show a general pattern of decreasing K_t with increasing L_f/L_{wave}. This indicates higher attenuation for the shorter waves, a trend that is consistent with observations for fixed submerged plates (Verduzco-Zapata et al., 2017; He et al., 2019). The breaking waves result in similar K_t to the non-breaking waves for $L_f/L_{waves} \geq 1$, but distinctly lower K_t for $L_f/L_{waves} < 1$. The latter marks a strongly nonlinear effect that relates to the intense plunging breaking for wave conditions REG10 and REG11 and illustrates that a breakwater that enforces wave breaking can lead to considerable wave attenuation. The reduction in wave transmission for these conditions is largely attributed to energy dissipation through breaking, although the breaking process may also affect the wave diffraction pattern around the structure.

Figure 9c shows the wave reflection coefficients K_r. Standard deviations were calculated by repeating the reflection analysis over three different combinations of upwave wave probes. K_r values vary with wave period and are in the range of 0 to 0.5, which is consistent with observations for dissipative parabolic beaches (Tiedeman et al., 2012). Reflection coefficients in the present study are also dependent on wave amplitude, with, for same wave period, lower wave reflection in the range of $0.9 < L_f/L_{wave} < 1.4$ but similar or higher K_r in the longer wave regime ($L_f/L_{wave} < 0.8$) for the higher-amplitude breaking waves.
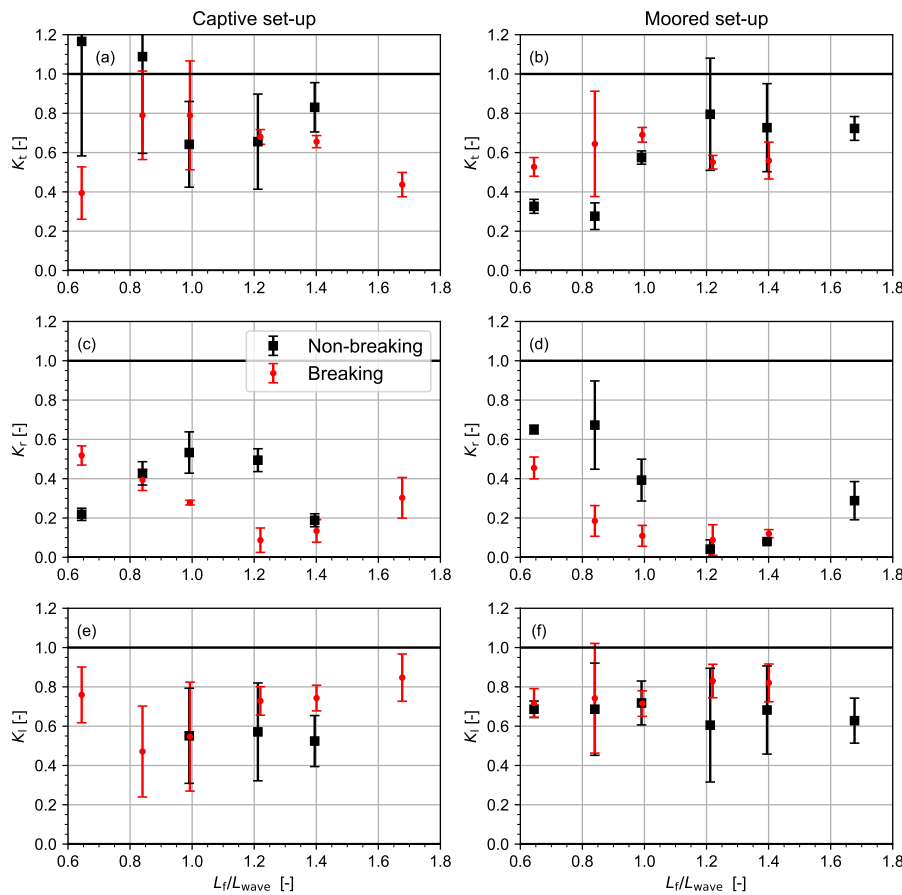

Figure 9: Wave transmission (upper), reflection (middle) and loss (bottom) coefficients for captive (left) and moored (right) setups: mean values (markers) $\pm$ 1 standard deviation (whiskers).

Finally, Figure 9e shows the loss coefficients. For the non-breaking cases, loss coefficients are primarily due to waves being diffracted into other directions than the lee-side of the floater. The breaking wave conditions follow the non-breaking wave data and are overall somewhat higher due to energy dissipation through breaking. K_l increases notably from condition REG10 ($L_f/L_{wave} = 0.84$) to REG11 ($L_f/L_{wave} = 0.66$), which is attributed to the more intense plunging breaking for the latter condition.

5.1.3 Wave transmission for moored setup

Transmission, reflection, and loss coefficients for the moored setup tests are presented in Table 4 and in Figure 9b,d,f. In terms of wave behaviour over the floater, the tests resulted again in non-breaking and breaking events. However, the breaking intensity for the moored setup tests was generally lower than for the captive setup tests (see also Table 4). This is explained by the breakwater moving along with the wave, especially through pitching of the floater, which apparently reduces the shoaling process and breaking intensity. Another notable difference to the captive setup tests is that in the moored setup, waves are not only reflected, dissipated, and transmitted, but are also radiated in various directions through motions of the floater.

Figure 9b shows the transmission coefficients for the moored setup. The non-breaking waves produce K_t of about 0.7 for $L_f/L_{wave} > 1$ and distinctly lower values for longer waves. The latter is explained by the waves with $L_f/L_{wave} < 1$ inducing strong pitching of the floater (see Section 4), resulting in more wave radiation and scattering of the wave field. The breaking wave conditions result in similar K_t to the non-breaking waves for $L_f/L_{wave} > 1$, but higher K_t for $L_f/L_{wave} < 1$. This is explained by the nonlinear pitch behaviour, with lower pitch RAOs for higher waves (Figure 5f), which in return, leads to relatively less wave radiation and higher transmission.

Figure 9d presents the wave reflection coefficients K_r, which in a moored setup are partly explained through radiated waves travelling in opposite direction to wave incidence. This explains the relatively high K_r for the non-breaking wave conditions with $L_f/L_{wave} \leq 1$. For the same wave lengths, the breaking wave conditions lead to lower K_r than the non-breaking waves, which is again attributed to the lower relative pitch response.

The loss coefficients in Figure 9f are the result of wave dissipation as well as diffraction and radiation to directions other than at lee side or upwave of the breakwater. Values are fairly similar across wave periods and wave heights; no evident differences between non-breaking and breaking cases are observed. This suggests that energy losses due to dissipation are less significant than 'losses' due to diffraction and radiation.

5.2 Irregular waves

The wave attenuation is further explored for irregular waves through Figure 10, which presents the wave spectra and water surface RAOs at lee side of the breakwater. Analogous to the motion RAOs and consistent with the adopted definition for the transmission coefficient K_t, the amplitudes of the water surface RAOs in [m/m] are calculated as the square root of the measured water surface spectrum normalized by the undisturbed wave spectrum. Results are shown for location $X/L_f = -1.32$, corresponding to the centre probe of the three wave probes used in the wave transmission analysis for regular waves.

For the captive setup tests (left-hand panels), the breakwater presence leads to a reduction in wave energy at wave lengths of $L_f/L_{wave} = 0.8$ to 1.5. Part of this energy is transferred towards lower frequencies ($L_f/L_{wave} = 0.4$ to 0.7; most evident for the white noise wave) and towards higher harmonics (most evident for JONS03 and JONS04). The water surface RAOs for the different wave conditions are closely aligned (Figure 10g) which suggests that the wave response at lee side of the breakwater is largely linear. This is explained because visually it was observed that for conditions WN up to JONS03, almost all waves passed the floater without breaking. An exception is the highest wave condition JONS04, in which about 5 to 10% of waves were observed to break (spilling and weakly plunging). This likely explains why the water surface response at $L_f/L_{wave} = 0.4$ to 0.7 is lower for JONS04 than for the other conditions. Note that the latter corresponds to relatively long waves, which are 'more shallow' above the breakwater (lower kh_0) and therefore more prone to shoaling and breaking than the shorter waves.
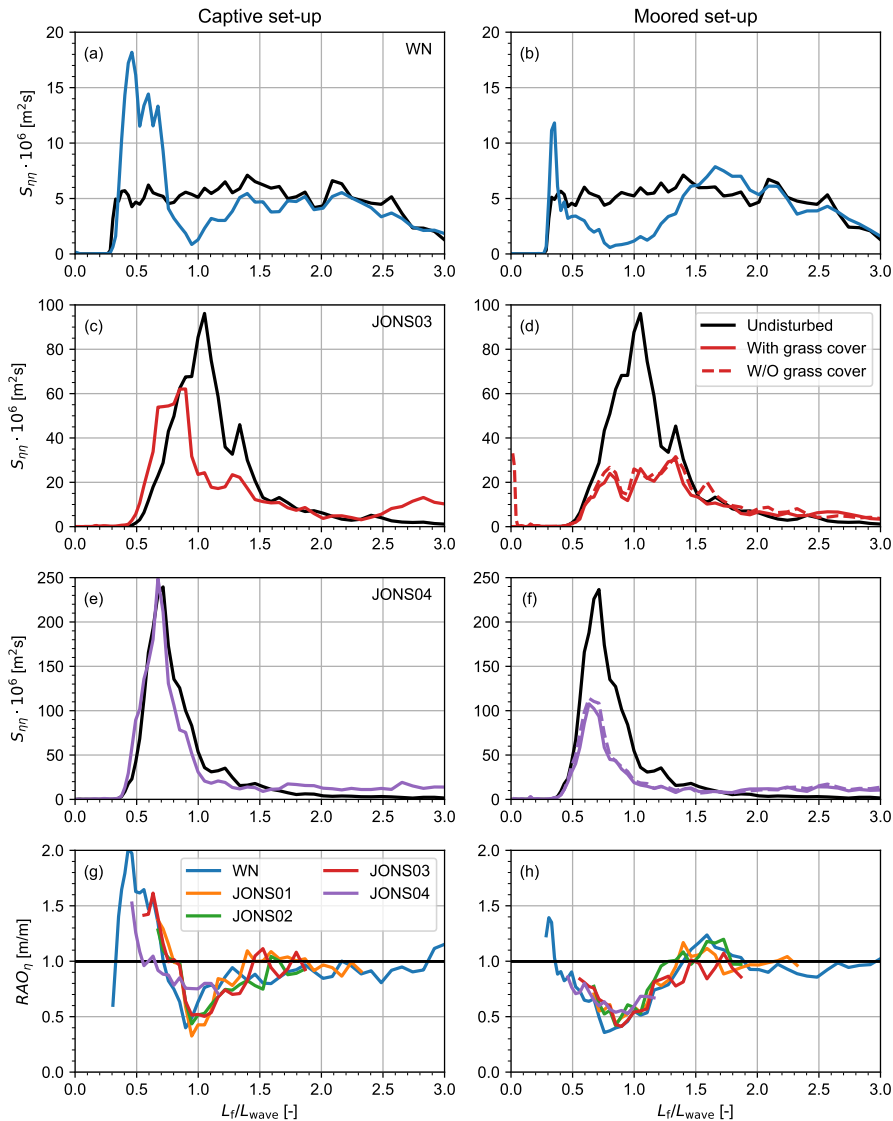
Figure 10: Water surface spectra (a-f) and normalized spectra (g-h) at $X/L_\mathrm{f} = -1.32$ for captive (left) and moored (right) setups in irregular waves. Water surface spectra are presented for conditions WN (a,b), JONS03 (c,d) and JONS04 (e,f), with black lines marking the undisturbed spectrum and coloured lines marking the spectrum at lee side of the breakwater. In panels (d, f) distinction is made between tests with (solid coloured) and without (dashed) grass cover.

Results for the moored setup are presented in the same figure at right-hand side. Compared to the captive setup, the reduction in wave energy is overall higher and covers a wider range of wave lengths ($L_\mathrm{f}/L_\mathrm{wave} = 0.3$ to 1.4). The reduction at longer wave lengths is primarily the result of wave radiation by the pitching floater. The water surface response RAOs are similar for all conditions, which suggests a linear response. This implies that for the tested wave conditions, wave attenuation is primarily the response of first-order processes (e.g., radiation) with higher-order processes such as shoaling and breaking being of secondary importance for the tested conditions, which did not result in intense plunging breaking. The comparison between captive and moored setup results illustrates that the attenuation performance depends strongly on the breakwater's motions and thus on its total stiffness (consistent with Loukogeorgaki and Angelides, 2005).

For waves JONS03 and JONS04, tests in moored setup were performed both with and without roughness layer at the top side of the floater. Both types of surface roughness lead to similar water surface RAOs (Figure 10c,f), which shows that the roughness layer has minor effect on wave attenuation.

6 Loads

This section presents the drift loads in regular waves (Section 6.1) and the mooring line loads in irregular waves (Section 6.2).

6.1 Total loads on floater

Total loads on the floater were measured through a 6-component force frame in captive setup and were derived from the mooring tensions for the moored setup tests (as described in Section 3.2.7). Time-averaged loads divided by the squared incident wave amplitude form the main diagonal of the quadratic transfer function (QTF), which is presented for the three degrees of freedom in Table 4. The drift load in surge direction is also shown in Figure 11. In this representation the measured forces were normalized by the horizontal force on a fully reflective wall:

$$F_{\mathrm{D,wall}} = \frac{1}{2}\rho_{\mathrm{w}}gW_{\mathrm{f}}a_{\mathrm{i}}^2 \tag{7}$$

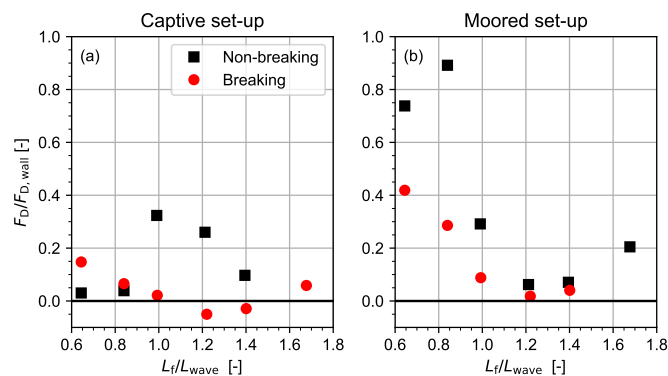Note that this expression is analogous to Eq. 2 with $K_{\mathrm{t}} = 0$.

Figure 11: Net surge drift loads for captive (a) and moored (b) setups.

In captive setup, highest F_{D} are induced by waves with $L_{\mathrm{f}}/L_{\mathrm{wave}} \approx 1$ to 1.2. Note that this corresponds to the waves that were also most strongly reflected (Figure 9c); the reversal of incident wave momentum upon the wave-structure interaction explains the relatively high drift load on the structure (see also Section 2.1). Interestingly, for the same relative wave lengths, the breaking wave conditions lead to much lower and in some cases even negative drift loads (i.e., net force in opposite direction to wave propagation). The negative drift loads are explained by the spatially varying water level set-down and set-up by wave shoaling and breaking. If the setup is located close to aft side of the structure, the reverse pressure gradient can exert a negative drift load on the object (Longuet-Higgins, 1977). This effect was anticipated in the breakwater design (see Section 2) and the present results confirm that the enforcing of wave breaking can indeed considerably reduce, and even reverse, wave drift loads. For the longest waves tested ($L_{\mathrm{f}}/L_{\mathrm{wave}} = 0.66$), the breaking waves induce slightly higher F_{D} than the non-breaking waves. This is again consistent with K_{r} measurements, which are also higher for the breaking wave condition at this relative wave length.

The loads in moored setup are generally higher than for the captive setup (Figure 11b). This relates firstly to the wave loads affecting the time-averaged position and orientation of the floater and secondly, to the first-order motions that affect the relative fluid velocities and accelerations, which in return alter the pressures and overall loads on the floater (Pinkster, 1979). For all tested wave conditions, the breaking waves induce relatively lower drift loads than the non-breaking waves. Similar to the captive setup results, this may again be related to reverse pressure gradients associated with wave breaking. Another explanation is that the non-linear damping results in a relatively lower first-order pitch motions for the (higher-amplitude) breaking wave conditions (Section 4), which in turn, affect the second-order drift loads.

The breakwater was designed to have a favourable balance between drift loads and wave attenuation. This balance is explored through Figure 12. Theoretical curves for reflective and dissipative breakwaters in 2D

---

conditions are included for reference. The non-breaking data would be expected to lie between the solid and dashed lines, because any reduction in transmitted wave energy is due to wave energy being either dissipated through friction or reflected. The reason why the non-breaking wave data are outside this expected region relates to 3D effects, with energy being diffracted towards other directions and with relatively high uncertainty in K_t estimates. Despite this uncertainty, the results indicate a distinctive difference in clustering between non-breaking and breaking wave conditions. For similar K_t levels, the breaking wave conditions lead to drift loads that are a factor two to five lower in magnitude than the non-breaking waves. This shows that the breakwater, for high waves that are enforced to break, has a more favourable balance between F_D and K_t than common breakwaters that attenuate wave energy through reflection or dissipation.
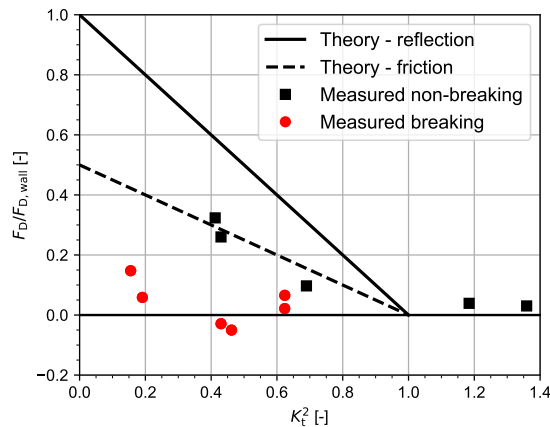

Figure 12: Drift loads versus transmission coefficient in regular waves and captive setup. Theoretical curves are provided for drift loads by reflective (solid line, Eq. 2) and dissipative (dashed line, Eq. 3) breakwaters.

6.2   Mooring line loads

Fluctuating mooring loads are explored through Figure 13a, which shows a time series excerpt of mooring tensions at fore and aft side for wave condition JONS03. Line tensions fluctuate both at wave frequencies and at lower frequencies. The wave frequency fluctuations at fore and aft side are typically in counter-phase, which indicates that these fluctuations result from pitch motions of the floater.

Time-varying loads for conditions JONS03 and JONS04 are further explored through their spectral distributions (Figure 13b,c). For wave condition JONS03, spectral distributions of line loads are similar at fore and aft side, which implies that the center of pitch rotation is roughly in the middle ($x \approx 0$) of the floater. For JONS04, the aft lines receive higher loads, which indicates a forward shift in the center of pitch rotation ($x > 0$). Most energy in line tensions fluctuations is observed at $L_f/L_{wave} = 0.4$ to 1.2, which is the result of pitch motions due to the short wave excitation. Spectral peaks are also observed around $L_f/L_{wave} \approx 0.08$ (natural frequency of heave) and a smaller peak around 0.20 (natural frequency of pitch). These results show that the pretension and first-order loads in the mooring lines make a substantial contribution to peak loads in the mooring lines, an observation that will be further addressed in the Discussion (Section 7).

For both wave conditions, the addition of a roughness layer (solid lines) on top of the floater reduces the mooring loads both at wave frequencies and at natural frequencies compared to a smooth top (dashed lines). The application of the grass cover reduced peak mooring loads during the tests by 15% and 18% for conditions JONS03 and JONS04, respectively. This is in line with the observations on the motion behaviour, which revealed a reduced motion response for the tests with grass cover due to the increased added mass and hydrodynamic damping (Section 4.2).
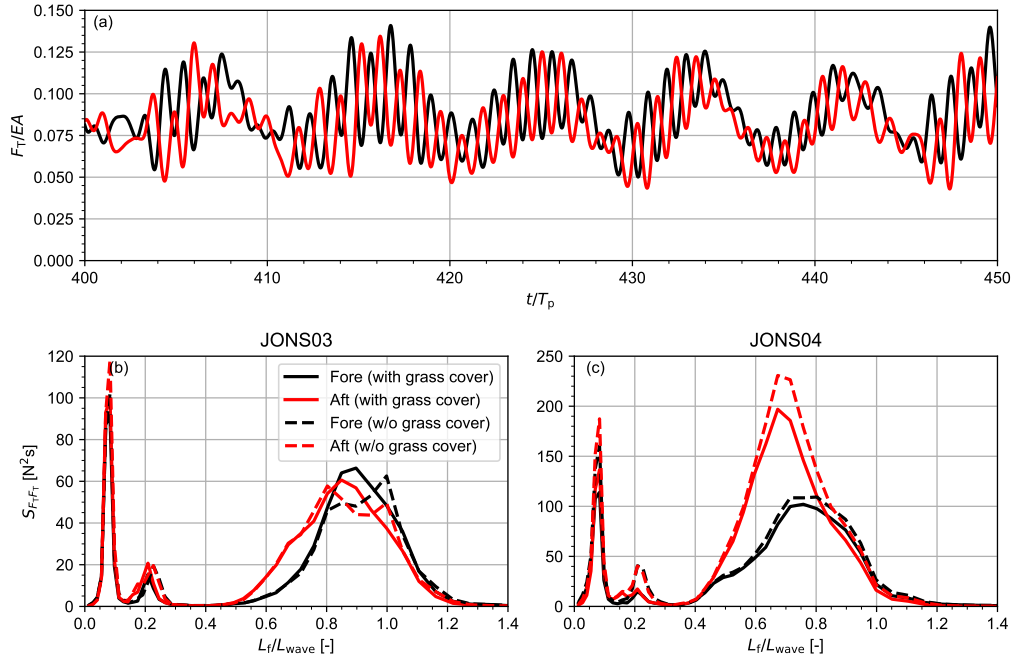
Figure 13: (a) Time series of average tension over mooring lines at fore (black) and aft (red) side for wave condition JONS03 (with roughness layer); (b-c) Spectra of mooring line tensions for JONS03 (a) and JONS04 (b) at fore (black) and aft (red) sides, for tests with (solid) and without (dashed) roughness cover on the floater.

7 Discussion

The present section compares the novel floating breakwater to existing designs, discusses the main pros and cons of the new design, and provides an outlook towards design improvement.

Common floating breakwater designs were introduced in Section 1. The most common design is the box-type floating breakwater which consists of a solid box that floats on the water surface (McCartney, 1985). For non-moving box-type breakwaters, assuming 2-D conditions and neglecting dissipation, the wave transmission coefficient can be expressed as function of water depth (h) and floater width ($W_{\rm f}$) and draft ($T_{\rm f}$) through the Macagno relation (Macagno, 1953; Burcharth et al., 2015):

$$K_{\rm t} = \frac{1}{\sqrt{1 + \left[\frac{kW_{\rm f}\sinh(kh)}{2\cosh(kh-kT_{\rm f})}\right]^2}} \tag{8}$$

Another common breakwater type is the pontoon-type (see Section 1), for which a modified version of Eq. 8 was proposed by Ruol et al. (2012). Figure 14 presents the theoretical $K_{\rm t}$ for box-type and pontoon-type breakwaters with same $W_{\rm f}, T_{\rm f}$ as the parabolic floater in the present study. The measured transmission coefficients for the present parabolic breakwater are consistently higher than the two theoretical curves. This shows that the parabolic breakwater is expected to attenuate less wave energy than common box- or pontoon-type breakwaters. This may be expected, because box- or pontoon-type breakwaters with same draft accommodate a much larger space of the water column than the present, relatively thin, submerged beach-shaped breakwater, and are effective in terms of blocking wave energy through reflection. The main advantages of the novel submerged parabolic breakwater design are therefore not found in terms of an improved attenuation performance, but instead, in the relatively low wave drift loads (Section 6) and its limited occupation of the water column (allowing water to pass beneath as well as over the floater).
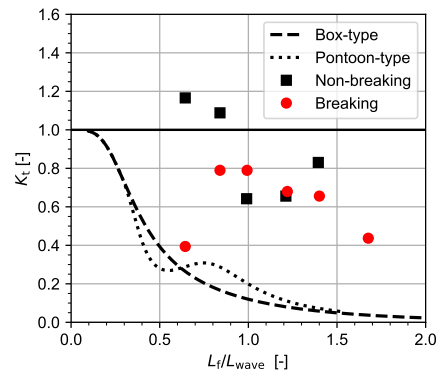
Figure 14: Transmission coefficients in regular waves and captive setup, including theoretical relations for motion-restrained box-type (Macagno, 1953) and pontoon-type (Ruol et al., 2012) floating breakwaters.

The hydrodynamic and structural design of the floater leaves room for further improvement. Firstly, the present floater is slender in vertical direction but it occupies a large horizontal area. As a result of the latter, heave and pitch motions will lead to considerable water displacement, which at shallow water may lead to scouring of the sea bed. In addition, the structure is expected to experience high bending moments while it has limited bending stiffness due to its relatively low thickness t_f. It is not evident up to which prototype scale the present design can be manufactured whilst guaranteeing its structural integrity. By increasing the floater's depth its structural strength could be improved, but at the expense of increasing wave loads. Alternatively, the floater length may be reduced, but this would alter the breakwater's attenuation performance and increase the first-order motions and second-order wave drift loads, hence increasing the costs of mooring. It is further noted that by lowering the floater position ($h_0 \neq 0$), the water depth above the floater does not satisfy the analytical formulation in Eq. 4. Because the parabolic curvature is subtle (see Figure 1), it is expected that a submerged plane slope would lead to similar performance as the present parabolic structure.

Another point for design improvement is the effective stiffness of the floater plus mooring. The principle of a wave breaking enforcing breakwater, as anticipated, leads to a favourable balance between wave attenuation and wave drift loads. At the same time, the moored setup resulted in reduced breaking intensity compared to the captive setup, which shows that high stiffness (limited floater motions) is required to promote energy dissipation through wave breaking. The present floating breakwater design is fully submerged and has no hydrostatic stiffness. Hence, all stiffness originate from the mooring lines, leading to pretension and first-order mooring loads that are relatively high (i.e., of similar magnitude as the second order fluctuating mooring loads, as follows from Figure 13). This could be overcome by extending the floater in vertical direction with columns that cross the waterline (similar to semi-submersibles). Such a solution would reduce the required pretension and first-order mooring loads, but at the cost of higher second-order drift loads (because of more wave reflection on the columns). Another option to increase the overall mooring stiffness would be to deploy and interconnect multiple floaters.

Above considerations illustrate the difficulties in designing a breakwater in terms of attenuation, motions, and mooring line tensions, especially because these design objectives tend to conflict. A decision framework as presented by Loukogeorgaki and Angelides (2005) for considering and evaluating these different design objectives may help to further improve the integral design of the floating breakwater (floater and mooring).

The authors foresee room for application of floating breakwaters both in coastal and offshore environments. In coastal regions, floating breakwaters may form an alternative or complimentary solution for coastal protection to more common practices of nourishments, hard structures, and forms of nature-based solutions, with added value especially in regions with fairly short waves and poor bottom foundation (McCartney, 1985; Burcharth et al., 2015). An advantage of floating breakwaters is that they can be easily removed and be used as a temporary solution, e.g., to support stabilization of vegetated shorelines. Floating breakwaters may therefore also be considered for areas protected by environmental conservation acts that pose restrictions on the construction of hard structures and the nourishing of external sediments. In offshore regions, floating breakwaters can help to secure complex operations (e.g., heavy lifting), form a shelter for permanent floating or bottom-fixed structures (e.g., wind parks), or be connected to large floating structures like floating modular islands (e.g., Flikkema and Waals, 2019; Drummen and Olbert, 2021; Tamis et al., 2021). For the latter application, a floating breakwater could be redesigned into a modular element that breaks and dissipates waves, resulting in a reduction of motions

and of total wave drift loads on the lee-side elements.

Synergy in side-functions of floating breakwaters can be found in roughness-enhancing elements such as shellfish or vegetation. The present results show that such rough elements may have marginal effect on the attenuation performance, but can increase the added mass and hydrodynamic damping and considerably reduce the breakwater's motions and peak mooring loads.

8   Conclusions

A new submerged floating breakwater design was presented. The novel breakwater is shaped as a parabolic beach and was designed to enforce breaking and promote dissipation of incident waves. Wave basin tests were performed with the breakwater in captive and moored setups. During these tests, the wave field, loads on the floater (captive setup), and motions and mooring loads (moored setup) were measured.

The wave attenuation performance of the breakwater depends on wave length, setup (captive vs. moored), and wave height. The latter marks a nonlinear response that was especially apparent when comparing breaking versus non-breaking waves with same wave period. Breaking waves resulted in lower wave transmission than non-breaking waves for the captive setup, but similar transmission was observed for the moored setup. Hence, a floating breakwater that enforces wave breaking has potential, but low motions and high hydrodynamic and mooring stiffness is required to enforce intense breaking. In moored setup, the wave attenuation is dominated by diffraction and radiation, with energy dissipation due to breaking being of secondary importance. This implies that a stiffer setup is favorable in terms of energy dissipation through wave breaking.

Time-averaged wave drift loads in both setups showed distinct differences between breaking and non-breaking waves, with generally lower and in some cases negative drift loads for the breaking conditions. The latter is explained by wave breaking driving a net set-down and set-up of the water level, which exerts a reverse pressure gradient on the floater. This shows that wave drift loads can be reduced by enforcing wave breaking over a structure, leading to a favourable balance between wave attenuation and wave drift loads. Compared to common box- or pontoon-type breakwaters, the new breakwater design is less effective in terms of attenuation but experiences lower wave drift loads, potentially reducing the costs of mooring.

The addition of an artificial grass cover to the floater has minor effect on the attenuation performance but it increases the added mass and hydrodynamic damping, resulting in reduced motions and peak mooring loads. This shows that floating breakwaters can benefit from multi-use functions that naturally enhance the surface roughness (e.g., shellfish or vegetation).

Acknowledgements

Author contributions (CRediT)

JvdZ: Conceptualization, Methodology, Formal Analysis, Investigation, Writing – original draft, Visualization, Project administration; AvdH: Conceptualization; Writing – review and editing; WO: Conceptualization; Writing – review and editing; FS: Conceptualization; Writing – review and editing; BW: FS: Conceptualization; Writing – review and editing; JdW: Conceptualization; Writing – review and editing.

Notations

Name	Symbol	Unit
Wave amplitude (first harmonic)	a	m
Incident wave amplitude	a_i	m
Reflected wave amplitude	a_r	m
Transmitted wave amplitude	a_t	m
Incident wave amplitude	a_i	m
Linearized damping coefficient	B_lin	-
Floater depth	D_f	m
Drift load	F_d	N
Surge load	F_x	N
Line tension	F_T	N
Pretension	$F_{\mathrm{T},0}$	N
Heave load	F_z	N
Acceleration due to gravity	g	m/s^2
Water depth	h	m
Minimum water depth above floater in still water	h_0	m
Regular wave height	H	m
Significant wave height	H_s	m
Wave number	k	rad/m
Reflection coefficient	K_r	-
Transmission coefficient	K_t	-
Floater length	L_f	m
Pitch moment	M_y	Nm
Quadratic transfer function	QTF	N/m^2, Nm/m^2
Response amplitude operator	RAO	-
Regular wave period	T	s
Floater draft	T_f	m
Natural period	T_n	s
Wave peak period	T_p	s
Design period parabolic floater	T_des	s
Local coordinates	x, y, z	m
Global coordinates	X, Y, Z	m
Floater X position in still water equilibrium	X_0	m
Floater width	W_f	m
Floater submerged weight	w_f	N
Water surface elevation	η	m
Water density	ρ	kg/m^3
Pitch angle	θ	deg

References

Beji, S. and Battjes, J. (1993). Experimental investigation of wave propagation over a bar. *Coastal Engineering*, **19**(1), 151–162. ISSN 0378-3839.

Blenkinsopp, C.E. and Chaplin, J.R. (2008). The effect of relative crest submergence on wave breaking over submerged slopes. *Coastal Engineering*, **55**(12), 967–974. ISSN 03783839.

Borsje, B.W., Wesenbeeck, B.K.V., Dekker, F., Paalvast, P., Bouma, T.J., Katwijk, M.M.V. and Vries, M.B.D. (2011). How ecological engineering can serve in coastal protection. *Ecological Engineering*, **37**(2), 113–122. ISSN 0925-8574.

Brebner, A. and Ofuya, A.O. (1968). Floating Breakwaters. In: *11th International Conference on Coastal Engineering*, volume I, 1055–1094. ISSN 0589-087X.

Buchner, B. (2006). The Motions of a Ship on a Sloped Seabed. In: *Volume 1: Offshore Technology; Offshore Wind Energy; Ocean Research Technology; LNG Specialty Symposium*, 339–347. ASMEDC. ISBN 0-7918-4746-2.

Buchner, B., van Dijk, A. and de Wilde, J. (2001). Numerical Multiple-Body Simulations of Side-by-Side Mooring to an FPSO .

Burcharth, H.F., Zanuttigh, B., Andersen, T.L., Lara, J.L., Steendam, G.J., Ruol, P., Sergent, P., Ostrowski, R., Silva, R., Martinelli, L., Nørgaard, J.Q.H., Mendoza, E., Simmonds, D., Ohle, N., Kappenberg, J., Pan, S., Nguyen, D.K., Toorman, E.A., Prinos, P., Hoggart, S., Chen, Z., Piotrowska, D., Pruszak, Z., Schönhofer, J., Skaja, M., Szmytkiewicz, P., Szmytkiewicz, M., Leont'yev, I., Angelelli, E., Formentin, S.M., Smaoui, H., Bi, Q., Sothmann, J., Schuster, D., Li, M., Ge, J., Lendzion, J., Koftis, T., Kuznetsov, S., Puente, A., Echavarri, B., Medina, R., Díaz-Simal, P., Rodriguez, I.L., Maza, M. and Higuera, P. (2015). Chapter 3 - innovative engineering solutions and best practices to mitigate coastal risk. In: B. Zanuttigh, R. Nicholls, J.P. Vanderlinden, H.F. Burcharth and R.C. Thompson (Editors), *Coastal Risk Management in a Changing Climate*, 55 – 170. Butterworth-Heinemann, Boston. ISBN 978-0-12-397310-8.

Cheng, Y., Ji, C., Ma, Z., Zhai, G. and Oleg, G. (2017). Numerical and experimental investigation of nonlinear focused waves-current interaction with a submerged plate. *Ocean Engineering*, **135**(March), 11–27. ISSN 00298018.

Christensen, E.D., Bingham, H.B., Skou Friis, A.P., Larsen, A.K. and Jensen, K.L. (2018). An experimental and numerical study of floating breakwaters. *Coastal Engineering*, **137**(March), 43–58. ISSN 03783839.

Dai, J., Ming, C., Utsunomiya, T. and Duan, W. (2018). Review of recent research and developments on floating breakwaters. *Ocean Engineering*, **158**(March), 132–151. ISSN 0029-8018.

Dong, G.H., Zheng, Y.N., Li, Y.C., Teng, B., Guan, C.T. and Lin, D.F. (2008). Experiments on wave transmission coefficients of floating breakwaters. *Ocean Engineering*, **35**(8-9), 931–938. ISSN 00298018.

Drimer, N., Agnon, Y. and Stiassnie, M. (1992). A simplified analytical model for a floating breakwater in water of finite depth. *Applied Ocean Research*, **14**(1), 33–41. ISSN 01411187.

Drummen, I. and Olbert, G. (2021). Conceptual design of a modular floating multi-purpose island. *Frontiers in Marine Science*, **8**, 86. ISSN 2296-7745. inserted by production after acceptance10.3389/fmars.2021.615222.

Faltinsen, O.M. and Loken, A.E. (1978). Drift Forces and Slowly Varying Forces on Ships and Offshore Structures in Waves. *Norw Marit Res*, **1**(6), 2–15.

Flick, R.E., Guza, R.T. and Inman, D.L. (1981). Elevation and velocity measurements of laboratory shoaling waves. *Journal of Geophysical Research*, **86**(C5), 4149–4160. ISSN 01480227.

Flikkema, M. and Waals, O. (2019). Space@sea the floating solution. *Frontiers in Marine Science*, **6**, 553. ISSN 2296-7745. inserted by production after acceptance10.3389/fmars.2019.00553.

Goda, Y. (2010). Reanalysis of regular and random breaking wave statistics. *Coastal Engineering Journal*, **52**(1), 71–106. ISSN 17936292.

Goda, Y. and Suzuki, T. (1976). Estimation of Incident and Reflected Waves in Random Wave Experiments. *Coastal Engineering Proceedings*, **1**(15), 47. ISSN 2156-1028.

Hales, L.Z. (1981). Floating Breakwaters: Stage-of-the-Art Literature Review. Technical report, US Army Corps of Engineers: Coastal Engineering Research Center.

He, F., Huang, Z. and Law, A.W.k. (2012). Hydrodynamic performance of a rectangular floating breakwater with and without pneumatic chambers : An experimental study. *Ocean Engineering*, **51**, 16–27. ISSN 0029-8018.

He, M., Gao, X., Xu, W., Ren, B. and Wang, H. (2019). Potential application of submerged horizontal plate as a wave energy breakwater: A 2D study using the WCSPH method. *Ocean Engineering*, **185**(March), 27–46. ISSN 00298018.

Huang, Z., He, F. and Zhang, W. (2014). A floating box-type breakwater with slotted barriers. *Journal of Hydraulic Research*, **52**(5), 720–727. ISSN 00221686.

Hughes, S.A. (1993). *Physical Models and Laboratory Techniques in Coastal Engineering.* World Scientific.

Jacobsen, N., McFall, B. and van der A, D. (2019). A frequency distributed dissipation model for canopies. *Coastal Engineering*, **150**, 135 – 146. ISSN 0378-3839.

Ji, C., Cheng, Y., Cui, J., Yuan, Z. and Gaidai, O. (2018). Hydrodynamic performance of floating breakwaters in long wave regime : An experimental study. *Ocean Engineering*, **152**(January), 154–166. ISSN 0029-8018.

Ji, C.y., Guo, Y.c., Cui, J., Yuan, Z.m. and Ma, X.j. (2016). 3D experimental study on a cylindrical floating breakwater system. *Ocean Engineering*, **125**, 38–50. ISSN 0029-8018.

Jonsson, I.G. (1980). a New Approach To Oscillatory Rough Turbulent Boundary Layers. *Ocean Engineering*, **7**, 109–152.

Koutandos, E.V., Karambas, T.V. and Koutitas, C.G. (2004). Floating Breakwater Response to Waves Action Using a Boussinesq Model Coupled with a 2DV Elliptic Solver. *Journal of Waterway, Port, Coastal, and Ocean Engineering*, **130**(5), 243–255. ISSN 0733-950X.

Liu, Z. and Wang, Y. (2020a). Numerical investigations and optimizations of typical submerged box-type floating breakwaters using SPH. *Ocean Engineering*, **209**(April), 107475. ISSN 00298018.

Liu, Z. and Wang, Y. (2020b). Numerical studies of submerged moored box-type floating breakwaters with different shapes of cross-sections using SPH. *Coastal Engineering*, **158**(March), 103687. ISSN 03783839.

Liu, Z., Wang, Y., Wang, W. and Hua, X. (2019). Numerical modeling and optimization of a winged box-type floating breakwater by Smoothed Particle Hydrodynamics. *Ocean Engineering*, **188**(July), 106246. ISSN 00298018.

Longuet-Higgins, M.S. (1977). Mean Forces Exerted By Waves on Floating or Submerged Bodies With Applications To Sand Bars and Wave Power Machines. *Proc R Soc London Ser A*, **352**(1671), 463–480.

Longuet-Higgins, M.S. and Stewart, R.W. (1964). Radiation stresses in water waves; a physical discussion, with applications. *Deep-Sea Research*, **11**, 529–562.

Loukogeorgaki, E. and Angelides, D.C. (2005). Stiffness of mooring lines and performance of floating breakwater in three dimensions. *Applied Ocean Research*, **27**(2005), 187–208.

Loukogeorgaki, E., Lentsiou, E.N., Aksel, M. and Yagci, O. (2017). Experimental investigation of the hydroelastic and the structural response of a moored pontoon-type modular floating breakwater with flexible connectors. *Coastal Engineering*, **121**(May 2016), 240–254. ISSN 03783839.

Macagno, E.O. (1953). Fluid mechanics – experimental study of the effects of the passage of a wave beneath an obstacle. In: *Proceedings of the Academic des Sciences.*

Maruo, H. (1960). The Drift of a Body Floating in Waves. *Journal of Ship Research*, **4**(3), 1–10.

McCartney, B.L. (1985). Floating breakwater design. *Journal of Waterway, Port, Coastal, and Ocean Engineering*, **111**(2), 304–318.

McGregor, R.C. and Gilbert, C.H.G. (1982). Floating Tyre Breakwaters – A Case History. In: *Coastal Engineering 1982*, volume 2, 1992–2008. American Society of Civil Engineers, New York, NY. ISBN 9780872623736.

Murali, K. and Mani, J.S. (1997). Performance of Cage Floating Breakwater. *Journal of Waterway, Port, Coastal, and Ocean Engineering*, **123**(4), 172–179. ISSN 0733-950X.

Pauw, W.H., Huijsmans, R.H.M. and Voogt, A. (2007). Advances in the Hydrodynamics of Side-by-Side Moored Vessels. In: *Volume 4: Materials Technology; Ocean Engineering*, 597–603. ASMEDC. ISBN 0-7918-4270-3.

Peña, E., Ferreras, J. and Sanchez-Tembleque, F. (2011). Experimental study on wave transmission coefficient, mooring lines and module connector forces with different designs of floating breakwaters. *Ocean Engineering*, **38**(10), 1150–1160. ISSN 00298018.

Peng, W., Lee, K.h., Shin, S.h. and Mizutani, N. (2013). Numerical simulation of interactions between water waves and inclined-moored submerged floating breakwaters. *Coastal Engineering*, **82**, 76–87. ISSN 0378-3839.

Peregrine, D.H. (1983). Breaking waves on beaches. *Annual review of fluid mechanics. Volume 15*, 149–178.

Phillips, O.M. (1960). On the dynamics of unsteady gravity waves of finite amplitude. *Journal of Fluid Mechanics*, **9**(02), 193–217.

Pinkster, J.A. (1979). Mean and low frequency wave drifting forces on floating structures. *Ocean Engineering*, **6**(6), 593–615. ISSN 00298018.

Postacchini, M., Brocchini, M., Corvaro, S. and Lorenzoni, C. (2011). Comparative analysis of sea wave dissipation induced by three flow mechanisms. *Journal of Hydraulic Research*, (July), 37–41.

Rahman, A., Mizutani, N. and Kawasaki, K. (2006). Numerical modeling of dynamic responses and mooring forces of submerged floating breakwater. *Coastal Engineering*, **53**, 799–815.

Ruol, P., Martinelli, L. and Pezzutto, P. (2012). Experimental and Numerical Investigation of the Effect of Mooring Stiffness on the Behaviour of Π -Type Floating Breakwaters. In: *ISOPE*, volume 500, 1–8.

Sarpkaya, T. and Isaacson, M. (1981). *Mechanics of Wave Forces on Offshore Structures*. Van Nostrand Reinhold Company Inc., New York. ISBN 0-442-25402-4.

Svendsen, I.A. (1984). Wave heights and set-up in a surf zone. *Coastal Engineering*, **8**, 303–329.

Svendsen, I.A. (1985). Physical Modelling of Water Waves. In: R.A. Dalrymple (Editor), *Physical Modelling in Coastal Engineering*, 13–47. A. A. Balkema, Rotterdam, The Netherlands.

Tamis, J.E., Jongbloed, R.H., Piet, G.J. and Jak, R.G. (2021). Developing an environmental impact assessment for floating island applications. *Frontiers in Marine Science*, **8**, 378. ISSN 2296-7745. inserted by production after acceptance10.3389/fmars.2021.664055.

Tang, H.j., Huang, C.c. and Chen, W.m. (2011). Dynamics of dual pontoon floating structure for cage aquaculture in a two- dimensional numerical wave tank Dynamics of dual pontoon floating structure for cage aquaculture in a two-dimensional numerical wave tank. *Journal of Fluids and Structures*, **27**(7), 918–936. ISSN 0889-9746.

Tiedeman, S., Allsop, W., Russo, V. and Brown, A. (2012). A demountable wave absorber for wave flumes and basins. In: *Proceedings of the 33rd International Conference on Coastal Engineering*.

van Steeg, P. and van Wesenbeeck, B.K. (2011). Large-scale physical modelling of wave damping of brushwood mattresses. Technical report, Deltares, Delft, Netherlands.

Verduzco-Zapata, M.G., Ocampo-Torres, F.J., Mendoza, E., Silva, R., Liñán-cabello, M. and Torres-orozco, E. (2017). Optimal submergence of horizontal plates for maximum wave energy dissipation. *Ocean Engineering*, **142**(June), 78–86. ISSN 0029-8018.

Verduzco-Zapata, M.G., Ocampo-Torres, F.J., Osuna, P., Parés-Sierra, A.F. and Kawasaki, K. (2012). Practical estimation of wave transmission and reflection from fixed submerged structures. *Ocean Engineering*, **45**, 63–74. ISSN 00298018.

Vuik, V., Borsje, B.W., Willemsen, P.W. and Jonkman, S.N. (2019). Salt marshes for flood risk reduction: Quantifying long-term effectiveness and life-cycle costs. *Ocean and Coastal Management*, **171**, 96 – 110. ISSN 0964-5691.

Walles, B. (2015). *The role of ecosystem engineers in the ecomorphological development of intertidal habitats Brenda Walles*. Phd thesis, Wageningen University.

Wright, L.D., Gammisch, R.A. and Byrne, R.J. (1990). Hydraulic roughness and mobility of three oyster-bed artificial substrate materials. *Journal of Coastal Research*, **6**(4), 867–878.

Zhang, X.S., Ma, S. and Duan, W.y. (2018). A new L type floating breakwater derived from vortex dissipation simulation. *Ocean Engineering*, **164**(May), 455–464. ISSN 00298018.

Zhao, X.L., Ning, D.Z., Zou, Q.P., Qiao, D.S. and Cai, S.Q. (2019). Hybrid floating breakwater-WEC system: A review. *Ocean Engineering*, **186**(June), 106126. ISSN 00298018.